Winter 12-2015

Investigation of 89Zr-Siderophores as Molecular Imaging Agents for Positron Emission Tomography Imaging of Bacterial Infections

Nora C. M. Goscinski
Washington University in St. Louis

WASHINGTON UNIVERSITY IN ST. LOUIS

Department of Chemistry

Investigation of ^{89}Zr-Siderophores as Molecular Imaging Agents for Positron Emission Tomography Imaging of Bacterial Infections

by

Nora Catharina Mary Goscinski

A thesis presented to the
Graduate School of Arts & Sciences
of Washington University in
partial fulfillment of the
requirements for the degree
of Master of Arts

December 2015
St. Louis, Missouri

Table of Contents

List of Figures

List of Tables

Acknowledgments

First and foremost, I would like to thank Dr. Suzanne Lapi for her generous financial support and for giving me the freedom to pursue my own projects and independently manage collaborations during my graduate work. I would be remiss if I did not also thank Dr. Timothy Wencewicz, both for collaborating on such an exciting project and for serving on my yearly committee, and Dr. Lee Sobotka, for serving on my committee and ensuring I accurately described the fine structure of whatever I discussed. All of you have been extremely valuable in my growth as a scientist. Thanks are also due to my undergraduate mentee, Samantha Kelly. Working with you has really helped me grow as a teacher as well as a scientist.

Thank you to the entire Lapi group for welcoming and supporting me during my graduate work. I'd like to specifically thank Paul Eisenbeis, without whom much of my ^{64}Cu work could not have been validated, Dr. Tolulope Aweda for her invaluable assistance in animal studies, and Drs. Brian Wright, Jennifer Burkemper and Bernadette V. Marquez for letting me tag along with "Team ^{89}Zr-herceptin". Many thanks are due to Kathryn Andel and Jan Francis for all their patient assistance with my administrative needs.

I'd like to thank my family for their help and support over the past two years. Special thanks are due to my sister, Philena, without whose emotional support I wouldn't have made it through the rough patches, and to Laura Conti, whose outside scientific opinion fruitfully contributed to solving many puzzles during my graduate work. Finally, I'd like to thank smy friends Noelle Elzas, Alicia Fleege, Elizabeth Abraham, and Kathryn and Adam Austin. You've given me a good deal of intellectual and emotional back-up over the past two years and I'm deeply grateful to know you.

Nora Goscinski

Washington University in St. Louis

September 2015

In memory of my grandparents, William and Ingeborg Burke

ABSTRACT OF THE THESIS

Investigation of ^{89}Zr-Siderophores as Molecular Imaging Agents for Positron Emission Tomography Imaging of Bacterial Infections

by

Nora Catharina Mary Goscinski

Master of Arts in Chemistry

Washington University in St. Louis, 2015

Professor Suzanne E. Lapi, Chair

Siderophores are small molecules synthesized by bacteria to harvest Fe^{3+} from their environment. In infection scenarios, their production can increase infection virulence by increasing the ability of bacteria to obtain Fe^{3+} and therefore grow more rapidly. The selective uptake of siderophores *in vivo* in multi-bacteria environments indicates that this class of molecules has a potential use as selective imaging agents. In this work, DFO-NCS and a library of trihydroxamate siderophores were evaluated as vehicles to deliver ^{89}Zr selectively to bacteria for Positron Emission Tomography (PET) imaging of bacterial infections.

Productive work with radiometals involves thorough knowledge of the element's chemistry as well as the sources and detrimental effects of any contaminating metal ions present with the radiometal in the reaction mixture. As a case study to determine the factors likely to interfere with the complexation of any given radiometal, the quality control assay used to determine effective specific activity (ESA) of ^{64}Cu was intensely examined. The purpose of this study was to identify sources of

cold metal contaminants in the ^{64}Cu production process and to identify which of those metals interfere with the binding of ^{64}Cu to the TETA chelator. The TETA titration method for determining ^{64}Cu ESA has relative standard deviations of 27.6% and 40.3% for repeatability and reproducibility respectively and the chelator TETA is selective for picomolar amounts of Cu^{2+} in the presence of low millimolar concentrations of Zn^{2+} and Ni^{2+}.

When the ^{89}Zr-DFO-NCS complex was tested against a panel of cell types, the uptake by human cells (SKBR3), *Staphylococcus aureus* cells, and *Pseudomonas aeruginosa* cells was significantly different ($p<0.0001$) and highest for *S. aureus*. The Zr chemistry and bacterial uptake behavior of a library of trihydroxamate siderophores was then evaluated and compared to that of DFO-NCS. The uptake of ^{89}Zr-DFO-NCS and a siderophore library member (^{89}Zr-V-129) were tested in a murine lung infection model (*P. aeruginosa*, PA M57-15) and the lung uptake of ^{89}Zr-V-129 was found to be significantly higher in infected mice ($p=0.012035$) than in control mice. The uptake of ^{89}Zr-DFO-NCS did not differ significantly between control and infected mice ($p=0.831$). ^{89}Zr-siderophores have been shown to possess potential to be selective, specific PET tracers for imaging bacterial infections *in vivo* and their utility for infection imaging should be more thoroughly explored.

Chapter 1: Introduction to Radiochemistry

While all chemists are familiar with the periodic table, which organizes the known elements by proton number and similarity of chemical behavior, nuclear and radiochemists have an additional reference available to them, the chart of the nuclides (*figure 1-1*, below). The chart of the nuclides can be thought of as an extended periodic table, where each box represents a single nucleus rather than the average elemental mass presented in each box of the periodic table. Proton number is plotted in the y-direction, neutron number in the x-direction, and a third quantity (mass) can be imagined to be plotted along the z-axis. The nucleus with lowest mass along an isobar (white arrow) is the most stable. The valley of stability (black boxes) runs approximately through the center of the nuclides, but bends 'south' as neutron number increases.

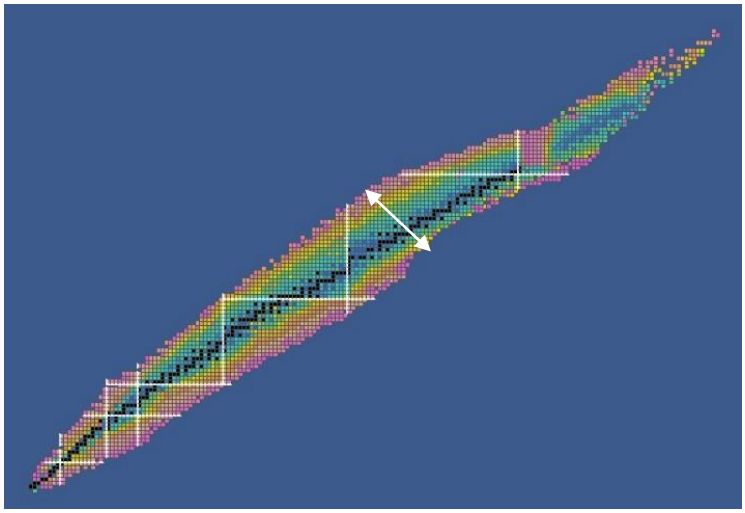

Figure 1: The Chart of the Nuclides[a]

[a] https://www-nds.iaea.org/relnsd/vcharthtml/VChartHTML.html

1.1 Types of Radioactive Decay

Unstable nuclei undergo radioactive decay when the daughter nucleus has a higher binding energy per nucleon than the parent nucleus [2]. Stated another way, a nucleus will undergo a particular mode of radioactive decay if the sum of the masses of particles after the decay is less than the initial mass of the unstable nucleus [2, 3]. However, nuclei may achieve this goal by a variety of routes. The three main modes of radioactive decay are alpha, beta (β^- ,β^+, or electron capture) and gamma emission. Although fission is a route by which certain unstable nuclei may reach stability, it will not be discussed in this work.

1.1.1 Alpha Decay

When a nucleus undergoes alpha decay, the parent nucleus ejects a helium nucleus (2 protons, 2 neutrons), also known as an alpha particle [2].

$$^{210}_{84}Po \rightarrow {}^{4}_{2}He + {}^{206}_{82}Pb \qquad \textbf{(1)}$$

The ejected α particle travels until it acquires 2 electrons and becomes an uncharged He atom. With a few key exceptions (such as ^{8}Be), nuclei that decay via alpha particle emission tend to be rather massive (A≥208 [3]) and are found at the upper end of the chart of the nuclides (high-Z, high-A nuclei) (*figure 1-1*).

1.1.2 Beta Decay

Most nuclei decay via one of the three modes of beta particle emission [2, 4]. Typically, nuclei below the valley of stability decay via β^- emission[2, 3]. In this decay mode, a neutron in the nucleus decays to a proton, an electron and an anti-neutrino:

$$^{90}_{39}Y \rightarrow {}^{90}_{40}Zr + \beta^- + \overline{\nu} \qquad \textbf{(2)}$$

The daughter nucleus ejects the electron and anti-neutrino and these ejecta travel until the electron is moving slowly enough to be incorporated into an atomic electron cloud. The anti-neutrino interacts minimally with matter and travels great distances.

Nuclei above the valley of stability decay are proton-rich and therefore decay via β^+ emission or electron capture. In β^+ emitting nuclei, a proton decays to a neutron, as well as a positron (β^+, the anti-matter of the electron) and a neutrino [2, 3]:

$$^{89}_{40}Zr \rightarrow {}^{89}_{39}Y + \beta^+ + \nu \qquad \textbf{(3)}$$

As in β^- decay, the daughter nucleus ejects the leptons, in this case the positron and neutrino. However, once the β^+ has lost sufficient energy to be captured, it is captured by an ordinary electron [3]. The captured β^+ may form a neutral complex (known as Positronium, Ps) with the capturing electron, or may immediately undergo annihilation [2]. The Ps complex is very short-lived and the β^+ and e^- soon annihilate one another, producing two γ photons (511 keV each) at ~180^0 relative to each other[b] [2, 3]. These two coincident photons are the basis of the nuclear imaging technique Positron Emission Tomography (PET, see section 1.3.3) [2, 3, 5].

A third mode of β decay, known as electron capture, occurs when the nucleus captures a low-energy atomic electron, transforming a proton into a neutron [2, 3]. Nuclei undergoing electron capture decay lie above the line of stability, but lack sufficiently large Q values (mass difference between nuclei on an isobar) to undergo positron decay [2].

[b] The angle between annihilation photons is not always precisely 180 degrees but this work makes the assumption that any variation in this angle is too small to drastically alter any results obtained from the study of positron-emitting nuclides *in vivo*.

1.1.3 Gamma Decay

Immediately after a nucleus decays by α or β emission, the daughter nucleus typically exists in a highly excited state [2, 3]. This excited daughter then relaxes to a lower-energy ground state via a variety of modes. Electromagnetic radiation is released from the daughter nucleus as a result of this relaxation. Such radiation originating from the nucleus is known as gamma (γ) radiation [2]. While γ emission does not result in a new element, it does result in a more stable nucleus. Often, the γ is emitted extremely close in time to the β decay event, but a few nuclides exist in which the emission of γ radiation by the excited daughter nucleus is delayed by minutes to hours [2]. These long-lived excited daughters are known as metastable isomers of a nuclide [2] and can be isolated from the parent material for use in applications requiring photons, such as medical imaging. A metastable isomer commonly used in medicine is ^{99m}Tc[4, 5], used in single photon emission computed tomography (SPECT)[4], which is produced according to the following (simplified) scheme:

$$^{99}_{42}Mo \rightarrow \beta^- + {}^{99m}_{43}Tc \rightarrow {}^{99}_{43}Tc + \gamma\ (140\ keV) \qquad \textbf{(4)}^{c}$$

The 140 keV γ photons given off by the relaxation of ^{99m}Tc to ^{99}Tc can be used to image disease within the body if attached to a suitable pharmaceutical [4, 5].

1.2 Production of Radioisotopes

There are two main routes by which radioisotopes are produced for research and clinical applications. Nuclei formed by neutron bombardment of the parent nucleus may be produced in

[c] ^{99}Mo is typically produced by the fission of ^{235}U in nuclear reactors.

nuclear reactors, while nuclides formed by proton bombardment of parent material may be produced using particle accelerators [2].

1.2.1 Nuclear Reactors

Nuclear reactors consist of rods of fissile uranium fuel (^{235}U) immersed in a neutron-slowing medium such as water or graphite (see *figure 1-2* for a schematic of a research reactor, below).

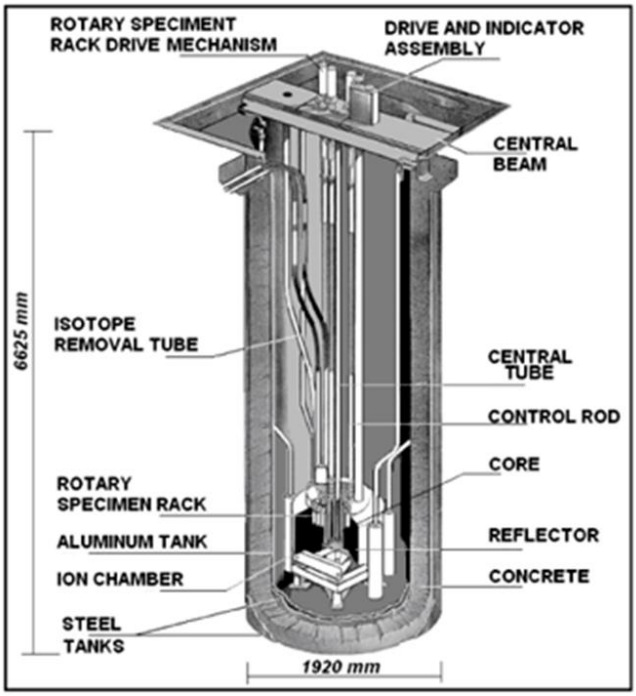

Figure 1-2: A typical "swimming pool" research reactor (a TRIGA IPR-R1) [6]

The fuel is arranged in a manner allowing a self-sustaining chain fission reaction to occur in a controllable manner [2, 3, 5]. Samples of the target material are typically sealed in quartz vials [2] and immersed in the reactor where they are bombarded by the sea of thermalized (slow) neutrons [2]. The capture cross section of the target nucleus is maximized at low average energies of incident neutrons, so 'slow' neutrons are most likely to induce nuclear reactions and transmute the parent into a daughter nucleus.

Because both parent and daughter have the same number of protons, the daughter is chemically identical to the parent material. This can make isolation of the pure daughter nucleus difficult, as

the parent and daughter can only be separated by physical methods, rather than by chemical means. Therefore, neutron irradiation in a nuclear reactor typically produces daughter nuclides with low specific activity (amount of radioactivity per unit mass) since large amounts of parent material remain with the daughter nuclide.

However, there are some cases (such as the production of ^{111}Ag from ^{110}Pd [7, 8]) in which the daughter formed by neutron bombardment is short-lived and decays via to a longer-lived, chemically distinct grand-daughter nuclide, allowing isolation of the ^{111}Ag with high specific activity. Radionuclides produced via neutron irradiation in nuclear reactors tend to lie below the valley of stability.

1.2.2 Accelerators

Isotopes produced via bombardment of a parent nucleus with charged particles may be produced in particle accelerators [2, 3]. While linear accelerators may be used to irradiate target materials [2], in practice most radioisotopes for biomedical imaging studies are produced in cyclotrons, which are more space-efficient [5]. A typical cyclotron is shown in *figure 1-3*, below.

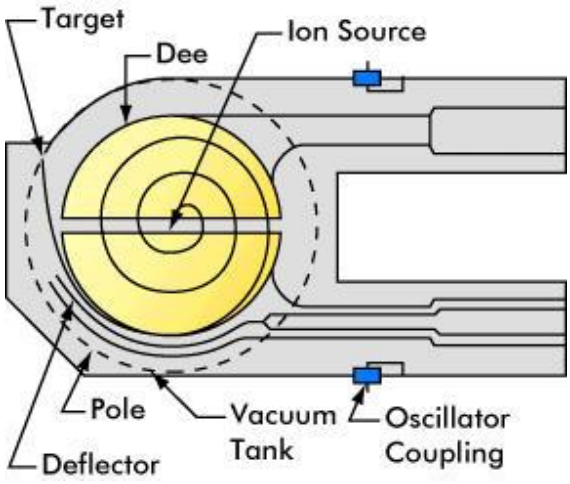

Figure 1-3: Cyclotron for production of radionuclides[d]

[d] http://www.daviddarling.info/encyclopedia/C/cyclotron.html

An ion source produces charged particles for acceleration; while these may be either cations or anions, a given machine will only use one. Under the influence of an electric field, the ions (typically H^-) move from the ion source to the electromagnets of the machine, where their path is curved by a magnetic field. When the ions reach the gap between the "dees" (charged plates between magnets), the electric field is reversed, accelerating the ions across the gap between dees [2, 5]. After this acceleration, the H^- have a higher energy and traverse a path longer than their original route within the dee, until they reach the gap between dees again. This process continues until the ions have achieved some maximum energy (dependent on the strength of the magnetic field and radius of the electrodes)[2, 4, 5]. When the H^- cannot be accelerated any further, they are routed through a stripper foil (to remove electrons and convert H^- to H^+), after which they curve out of the dee structure. The H^+ then bombard the target, reacting with nuclei and transmuting target nuclei into chemically distinct product nuclei[2]. Typically, this initial product nucleus is an extremely short-lived compound nucleus that evaporates at least one nucleon in order to achieve a more stable configuration of protons and neutrons[4]. It is this final product nucleus that is isolated from the target after irradiation. Radionuclides of medical interest produced by this method include ^{18}F, ^{64}Cu, ^{89}Zr, and ^{11}C (*Table 1-1*)

Table 1-1: Commonly used medical radionuclides and their production methods

Radionuclide	**Production Reaction**
^{18}F	${}^{18}_{8}O(p,n){}^{18}_{9}F$ [9]
^{11}C	${}^{14}_{7}N(p,\alpha){}^{11}_{6}C$ [10]
^{64}Cu	${}^{64}_{28}Ni(p.n){}^{64}_{29}Cu$ [11, 12]
^{89}Zr	${}^{89}_{39}Y(p,n){}^{89}_{40}Zr$ [13]

Radionuclides produced by charged particle irradiation typically lie above the valley of stability. They may decay by β^+ or EC emission, depending on the parent nucleus irradiated.

1.2.3 Comparison of Methods

Target irradiations in accelerators and in reactors are complementary methods of radionuclide production. As positron emission only occurs in nuclei above the line of stability, isotopes used in PET are produced on charged-particle accelerators[5]. However, nuclei below the line of stability are usually produced in nuclear reactors and these nuclides are often crucial for imaging and radiotherapy. The most commonly used isotope in nuclear medicine (^{99m}Tc) is produced from a reactor-derived parent (^{99}Mo).

1.3 Molecular Imaging

Molecular imaging can be defined as the study and application of molecules and machinery that permit non-invasive examination of biological processes in living organisms, rather than mere structural information[14]. While the most obvious application of molecular imaging is in the diagnosis and monitoring of disease, it can also be used to examine healthy biological systems. At its heart, molecular imaging is the quest to "see" specific chemical and biological processes and act on the information gleaned from said observation.

1.3.1 Glossary

To simplify the discussion, the following definitions will be used throughout this work:

Tracer: An entity, usually a molecule, that can be introduced to a living system and whose movement within that living system can be observed non-invasively.

Beacon: The part of the tracer responsible for the signal observed from outside the subject. For example, it may be a colored or fluorescent dye, a magnetically active metal ion or a radioactive atom.

Targeting moiety: The part of the tracer that binds to a specific biological structure or causes the tracer as a whole to behave in a particular manner.

1.3.2 The Tracer Principle

While not true for all imaging modalities, many molecular imaging techniques rest on a statement known as "the tracer principle". In its simplest form, this principle states that molecules used to probe biological systems do not perturb the system under observation provided the tracer concentration is sufficiently low. Furthermore, it assumes that molecules altered to be detectable through non-invasive methods (tracers) behave in a biologically identical manner to the unaltered molecules [2, 5]. This assumption is not strictly true, but in some imaging modalities, the difference between labeled and unlabeled tracer behavior is so small it can effectively be ignored[5].

1.3.3 Positron Emission Tomography

One of these methods is Positron Emission Tomography (PET). PET relies on detection of the coincident 511 keV γ photons produced by the annihilation of a β^+ with an ordinary electron[2]. Tracers used for this imaging modality must therefore contain atoms which decay via β^+ emission. The operating principle of a typical PET scanner is shown below, in *figure 1-4*. When two detectors in the ring detect an event simultaneously, the event is tagged as a coincidence event, and the tracer is assumed to lie along the line between the two detectors [2] (known as the line of response, LOR). Detection of many LOR's allows the exact location of the tracer within the system (typically a human patient) to be determined [5].

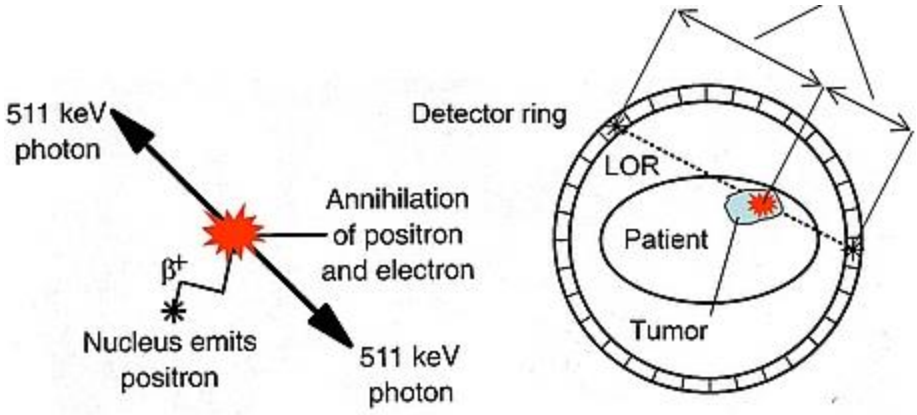

Figure 1-4: Positron Emission Tomography apparatus[e]

PET is a very sensitive technique [15]. The concentration of contrast agent in the body is usually 10^{-12} mols/L or lower after injection [16, 17], so it does not measurably perturb the biological functions observed via PET. Additionally, the beacon attached to the targeting moiety is extremely small (a single atom), so it is unlikely to alter the tracer's pharmacokinetic behavior *in vivo.* Because radioactivity is the signal monitored in PET, nearly background-free measurements are possible as essentially no positron-emitting nuclides are naturally present in the body[f] . Background-free images are easier to interpret, since any signal present is from the administered tracer, rather than from an endogenous entity. Finally, PET is a functional imaging modality, rather than an anatomical one. Instead of showing what tissues and structures are present, PET scans present information about the chemical and biological state of the system imaged [5]. Thus, chemical pathways specific to the target can be probed and information about processes occurring in the system can be obtained.

[e] Source http://www.tnw.tudelft.nl/en/about-faculty/departments/radiation-science-technology/research/particle-therapy/turning-the-physical-advantages-of-protons-into-true-clinical-benefits-with-in-beam-tof-pet/

[f] The exception is ^{40}K, which has a β^+ fraction of $1.0x10^{-3}$ % and a half-life of $1.25x10^{9}$ years [17].

1.3.4 Representative PET Isotopes

The PET isotopes in most common clinical use are ^{18}F and ^{11}C [4]. These nuclides are commonly incorporated into the structure of small organic molecules such as glucose (making [^{18}F]FDG). These tracers have short biological half-lives (due to their small size), and many have high-abundance targets *in vivo*, making the relatively short-lived ^{18}F and ^{11}C ideal candidates for radiolabeling. Both ^{11}C [19] and ^{18}F [20] emit low energy β^+ particles with no γ emissions other than the annihilation photons, giving rise to clear PET images with minimal radiation dose to the patient.

However, many imaging targets, e.g., cancer-specific receptors, are found in far lower abundance in the body than glucose transport proteins and require tracers with longer blood circulation times, such as monoclonal antibodies. Tracers with long biological $t_{1/2}$ require radiolabeling with longer-lived nuclides, so useful information may be extracted from imaging with these compounds [13]. Many of the longer-lived PET isotopes are radiometals. Emerging radiometals include ^{64}Cu[11, 12, 21-32] and ^{89}Zr [13, 32-43], both of which have been used to label antibodies (and other tracer types) and image disease within the human body.

1.3.5 Medical Uses of PET Tracers

The most common clinical use of PET is to examine global glucose uptake in patients[46]. Elevated glucose uptake is known to occur in diseased sites within a patient. Hypermetabolic cells (which take up more glucose than their neighbors) may be inflamed, infected or cancerous (the Warburg effect) [47-49]. A PET scan with [^{18}F]FDG will detect many of these pathologies[46]. However, [^{18}F]FDG cannot distinguish among the various conditions that underlie the increased glucose utilization of pathological cells[50]. There is a need to develop higher-specificity tracers that are taken up by narrow ranges of diseased cell types.

A novel use of PET that has been gaining attention in recent years is for imaging bacterial infections. The dynamics of bacterial infections and possible imaging targets specific to this disease type will be discussed in further chapters of this work.

1.4 References

1. Friedlander, G., Kennedy, J., Macias, E., and Miller, J. *Nuclear and Radiochemistry*. 3 ed. 1981, New York: John Wiley and Sons.

2. Sarantites, D. G., and Sobotka, L.G. *Chemistry 436: Introduction to the Atomic Nucleus* in *An Introductory One-Semester Course (Lecture Notes)*. 2013: St. Louis, MO.

3. Loveland, W., Morissey, D., and Seaborg, G. *Modern Nuclear Chemistry*. 1st ed. 2006, Hoboken, NJ: John Wiley and Sons.

4. Ehmann, W., and Vance, D. *Radiochemistry and Nuclear Methods of Analysis*. Chemical Analysis, ed. J.D. Winefordner. Vol. 116. 1991, New York: John Wiley and Sons. 531.

5. Zangirolami, D., de Oliveira, A., and Ferreira, A. *Thermal and Epithermal Neutron Fluence Rates in the Irradiation Facilities of the TRIGAIPR-R1 Nuclear Reactor.* Brazilian Journal of Physics, 2010. **40**(1): p. 47-51.

6. Neves, M., Kling, A., and Lambrecht, R. *Radionuclide production for therapeutic radiopharmaceuticals.* Applied Radiation and Isotopes, 2002. **57**(5): p. 657-664.

7. Chattopadhyay, S., et al., *Preparation and evaluation of a new radiopharmaceutical for radio synovectomy, Ag-111-labelled hydroxyapatite (HA) particles.* Applied Radiation and Isotopes, 2008. **66**(3): p. 334-339.

8. Liu, Y.-H., et al., *A study on the [18F]FDG production efficiency of the MINItrace™ cyclotron in Shin Kong Memorial Hospital.* Nuclear Instruments and Methods in Physics Research Section A: Accelerators, Spectrometers, Detectors and Associated Equipment, 2006. **562**(2): p. 1064-1067.

9. Adloff, J. and Guillaumont, R. *Fundamentals of Radiochemistry*. 1993, Boca Raton, FL: CRC Press.

10. Smith, S.V., *Molecular imaging with copper-64.* J Inorg Biochem, 2004. **98**(11): p. 1874-901.

11. McCarthy, D.W., et al., *Efficient production of high specific activity Cu-64 using a biomedical cyclotron.* Nuclear Medicine and Biology, 1997. **24**(1): p. 35-43.

12. Deri, M.A., et al., *PET imaging with 89Zr: From radiochemistry to the clinic.* Nuclear Medicine and Biology, 2013. **40**(1): p. 3-14.

13. *What are molecular imaging and nuclear medicine?* [Webpage] [cited 2015 16 June 2015]; SNMMI's website, containing their definition of molecular imaging]. Available from: http://www.snmmi.org/AboutSNMMI/Content.aspx?ItemNumber=6433.

14. Rahmim, A. and Zaidi, H. *PET versus SPECT: strengths, limitations and challenges.* Nuclear Medicine Communications, 2008. **29**: p. 193-207.

15. Spanoudaki, V. and Ziegler, S., *PET & SPECT Instrumentation*, in *Molecular Imaging I*, W. Semmler and M. Schwaiger, Editors. 2008, Springer Berlin Heidelberg. p. 53-74.

16. Wehrl, H. *et al., Combined PET/MR: A Technology Becomes Mature.* Journal of Nuclear Medicine, 2015. **56**(2): p. 165-168.

17. Singh, B., and Cameron, J.A., Nuclear Data Sheets, 2004. **102**: p. 293.

18. Kelley, J.H, Sheu, C.G., Nuclear Physics A, 2012. **880**: p. 88.

19. Tilley, Weller, Cheves, Chasteler, Nuclear Physics A 1995. **595**: p. 1.

20. Kume, M., et al., *A semi-automated system for the routine production of copper-64.* Appl Radiat Isot, 2012. **70**(8): p. 1803-6.

21. Marquez, B.V., et al., *Development of a Radio labeled Irreversible Peptide Ligand for PET Imaging of Vascular Endothelial Growth Factor.* Journal of Nuclear Medicine, 2014. **55**(6): p. 1029-1034.

22. Mastren, T., et al., *Specific activity measurement of (6)(4)Cu: a comparison of methods.* Appl Radiat Isot, 2014. **90**: p. 117-21.

23. Qaim, S.M., *Development of novel positron emitters for medical applications: nuclear and radiochemical aspects.* Radiochimica Acta, 2011. **99**(10): p. 611-625.

24. Handley, M.G., et al., *Cardiac hypoxia imaging: second-generation analogues of 64Cu-ATSM.* J Nucl Med, 2014. **55**(3): p. 488-94.

25. Handley, M.G., et al., *PET imaging of cardiac hypoxia: opportunities and challenges.* J Mol Cell Cardiol, 2011. **51**(5): p. 640-50.

26. Zeglis, B.M., et al., *Underscoring the influence of inorganic chemistry on nuclear imaging with radiometals.* Inorg Chem, 2014. **53**(4): p. 1880-99.

27. Hickey, J.L. and Donnelly, P.S., *Diagnostic imaging of Alzheimer's disease with copper and technetium complexes.* Coordination Chemistry Reviews, 2012. **256**(19-20): p. 2367-2380.

28. Hickey, J.L., et al., *Diagnostic imaging agents for Alzheimer's disease: copper radiopharmaceuticals that target Abeta plaques.* J Am Chem Soc, 2013. **135**(43): p. 16120-32.

29. Tavare, R., et al., *Enhanced immunoPET of ALCAM-positive colorectal carcinoma using site-specific 64Cu-DOTA conjugation.* Protein Eng Des Sel, 2014.

30. Viola-Villegas, N.T., et al., *Understanding the pharmacological properties of a metabolic PET tracer in prostate cancer*. Proceedings of the National Academy of Sciences of the United States of America, 2014. **111**(20): p. 7254-7259.

31. Zhou, Y., Baidoo, K.E., and Brechbiel, M.W., *Mapping biological behaviors by application of longer-lived positron emitting radionuclides.* Adv Drug Deliv Rev, 2013. **65**(8): p. 1098-111.

32. Leung, K., *[18F]Fluoro-2-deoxy-2-D-glucose.* 2005, National Center for Biotechnology Information (US): Bethesda, MD.

33. Warburg, O., *The Chemical Constitution of Respiration Ferment.* Science, 1928. **68**(1767): p. 437-443.

34. Chen, X., Qian, Y., and Wu, S., *The Warburg effect: Evolving interpretations of an established concept.* Free Radical Biology and Medicine, 2015. **79**(0): p. 253-263.

35. Warburg, O., Wind, F. and Negelein, E., *THE METABOLISM OF TUMORS IN THE BODY.* The Journal of General Physiology, 1927. **8**(6): p. 519-530.

36. *Diagnostic Imaging of infections and inflammatory diseases: a multidisciplinary approach*, A.M.Q. Alberto Signore, Editor. 2014, John Wiley and Sons.

Chapter 2: Bacterial Infections

2.1 Why Image Bacterial Infections?

The current diagnostic paradigm for patients appearing to have bacterial infections is time-consuming, requiring samples from the patient to be cultured for hours to weeks before enough bacteria are isolated to run destructive diagnostic tests [1]. The disease-causing bacteria are then usually identified through a combination of their growth requirements, dye uptake and enzymatic assays (such as whether the culture produces catalase)[1] (*figure 2-1).* Because proper identification of the disease often takes a long time and bacterial infections tend to progress rapidly (e.g., *Yersinia pestis* infections are fatal in 3-5 days if left untreated [1]), more-rapid diagnostic techniques would allow physicians to identify what types of antimicrobial therapy would help a patient in a clinically-relevant timeframe.

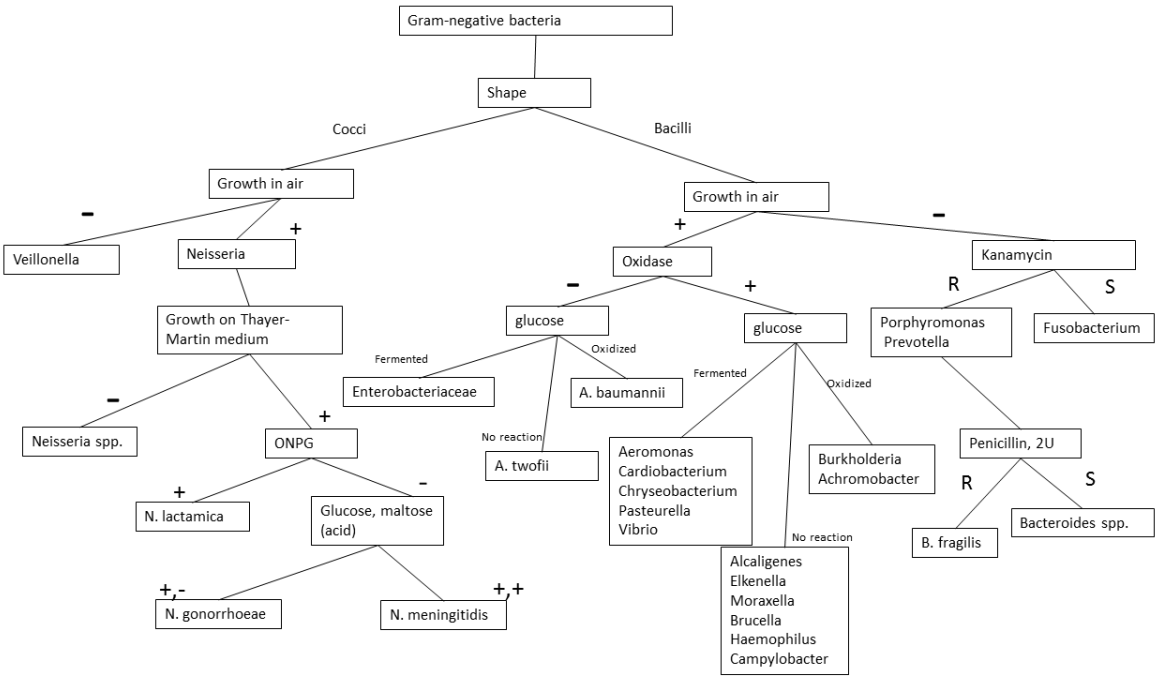

Figure 2-1: Typical identification of an unknown bacterium from clinical sample (adapted from [51])

The ability to image bacterial disease and identify the pathogen from imaging results would permit rapid, specific diagnosis of infection (as opposed to some other disorder causing illness) with a particular infectious agent. Identifying the bacterium causing a patient's disease would allow clinicians to administer narrow-spectrum antibiotics targeted at the pathogen, eliminating disease without also killing off "innocent bystanders" or potentially contributing to the rise of drug-resistant bacterial strains [1, 2]. Additionally, the ability to specifically image infections would allow long-term monitoring of infection progress and patient response to therapy, allowing clinicians to determine whether a treatment is truly curing a patient's disease or merely alleviating its symptoms.

2.2 The Role of Iron in Infection Dynamics

In humans, the Fe^{3+} ion is used as a co-factor in a variety of proteins and enzymes [3-5]. The common biological use of iron is as an oxygen carrier in hemoglobin and myoglobin. However, Fe is also used as a redox center by cytochrome proteins in the electron transport chain, which is responsible for most of a cell's ATP production, as well as in the enzyme holo-aconitase in the TCA cycle [5, 6]. Fe is also involved in cellular signaling, via the NO signal transduction pathway[3].

Bacteria likewise also require iron to carry out basic life processes, such as ATP synthesis. The bacterial electron transport chain uses cytochrome proteins with iron redox centers [7] and certain anaerobic bacteria can use Fe^{3+} as a terminal electron acceptor [7]. Additionally, iron is used as a redox cofactor for processes such as nucleotide synthesis [7, 8].

Iron availability is a crucial determinant of bacterial virulence [4, 7, 9]. Bacterial cells need to obtain iron from their environment in order to grow and divide within the host, to form biofilms and to lyse host cells, among other activities associated with virulence [1, 7, 10].

Because iron is so crucial to proper cellular function in both humans and bacterial cells, the human body has many systems to control the movement and use of iron [4, 9, 11]. Bacteria have evolved iron-harvesting systems that attempt to evade or outwit the host's attempt to withhold iron from invading cells [4, 7, 10-12]. Consequently, the ability of a bacterium to obtain iron from its environment is crucial to the successful establishment of infection.

2.3 Host Response to Infection

The human host's response to invasion by bacteria has two components. The innate immune system controls the pathways that are constitutively "on", while other portions are only activated in response to inflammation or infection-specific stimuli (such as the expression of particular cytokines, or pathogen-synthesized molecules) [1, 9]. A key strategy of both components of the immune response is to withhold iron from the infectious agent [4].

2.3.1 Constitutive Iron Sequestration

Iron in use *in vivo* is enclosed within many layers of biochemical structures [4, 6, 13]. For example, the Fe^{3+} used to carry O_2 in the blood is not merely complexed by heme. Heme groups nestle inside hemoglobin, and many units of hemoglobin are contained within each erythrocyte (red blood cell) [6, 13]. Therefore, many systems must fail before the Fe^{3+} ion is found in the blood. When erythrocytes die or are lysed, additional proteins are recruited to sequester the iron [4, 6, 10-13]. Free hemoglobin is complexed by haptoglobin and the resulting complex is shuttled to the spleen for recycling [10, 14]. Likewise, if heme is found outside hemoglobin, a protein called

hemopexin complexes the Fe-porphyrin ring and shuttles it to the reticuloendothelial system for recycling [10-11].

If Fe^{3+} manages to escape from heme, proteins circulating in the blood can bind the ion, reducing the concentration of free Fe^{3+} in the blood. Some of these proteins are specifically designed to chelate and transport Fe^{3+}, such as transferrin (Tf) [4, 6, 12, 13], while others such as albumin are general "workhorse" transport proteins capable of binding many entities [4, 6]. If the plasma proteins are unavailable for binding Fe^{3+}, the free metal can be complexed by small molecules in the blood plasma such as citrate and free amino acids [4, 14].

An additional word should be said regarding the role of transferrin. Transferrin is a small (80 kDa) glycoprotein ordinarily found in the blood and cerebrospinal fluid whose role is to chelate and transport Fe^{3+} to tissues where it is needed [3, 15]. It is internalized by endocytosis and releases Fe^{3+} in the low-pH endosome before being excreted for another round of Fe^{3+} transport [3]. Because the pH of the blood, CSF and interstitial fluid is approximately neutral (pH 7.4) [16], Fe^{3+} is unlikely to be released in an uncontrolled manner in healthy hosts. These fluids are normally sterile. However, fluids which can contact the air (such as tears, saliva, bile and breast milk) utilize a different iron transport protein. These fluids tend to have a lower pH than blood [1] and also may encounter bacteria. An iron transport protein that releases Fe^{3+} under acidic conditions would encourage bacterial growth in these fluids, so the protein lactoferrin (Lf) is used to bring iron to cells in contact with these fluids [4, 6, 9, 11, 13]. Lactoferrin does *not* release Fe^{3+} under acidic conditions and therefore can traffic Fe^{3+} to epithelial tissues without making the iron available to bacteria or fungi that may be present near these tissues [4, 9, 10, 12, 14].

2.3.2 Infection Response Pathways

Should an infection establish itself in the body, the liver responds to inflammatory cytokines [9] by producing the peptide hormone hepcidin [4, 6, 9, 10, 12]. Hepcidin suppresses the production of ferroportin, a cation transport protein used to bring Fe^{3+} into the cytosol [4, 12]. Ferroportin production is particularly suppressed in cells lining the GI tract, reducing iron absorption from the diet [12].

Bacteria tend to acidify tissues they infect (mainly to generate the proton gradient necessary for oxidative phosphorylation), so any Fe^{3+} in the area bound by transferrin (Tf) will be released to solution and thus made available to the pathogens. Therefore, empty lactoferrin is trafficked to the infected or inflamed site to scavenge any free Fe^{3+} in the area [4, 10-13].

2.4 Bacterial Response to Iron Sequestration

Bacteria have evolved many mechanisms to scavenge iron from their environment, whether that environment is a human host or a matrix such as soil. These mechanisms include lysing erythrocytes to internalize and degrade hemoglobin [6, 10, 13], internalizing and degrading Fe-transferrin and Fe-lactoferrin [4, 10, 11, 13], lowering the pH of their environment to promote Fe^{3+} dissociation from Tf [10, 12], and siderophore production [4, 6, 9-11, 13]. This last pathway is interesting from a chemical and molecular imaging perspective.

2.4.1 The Siderophore Pathway

Siderophores are small molecules synthesized and excreted by bacteria (and some fungi) to harvest Fe^{3+} from their environment [4, 6, 9-11, 13] (*figure 2-2*). They bind Fe^{3+} with extremely high affinity (binding constants on the order of ~10^{50} [14, 17]) but bind Fe^{2+} poorly, if at all.

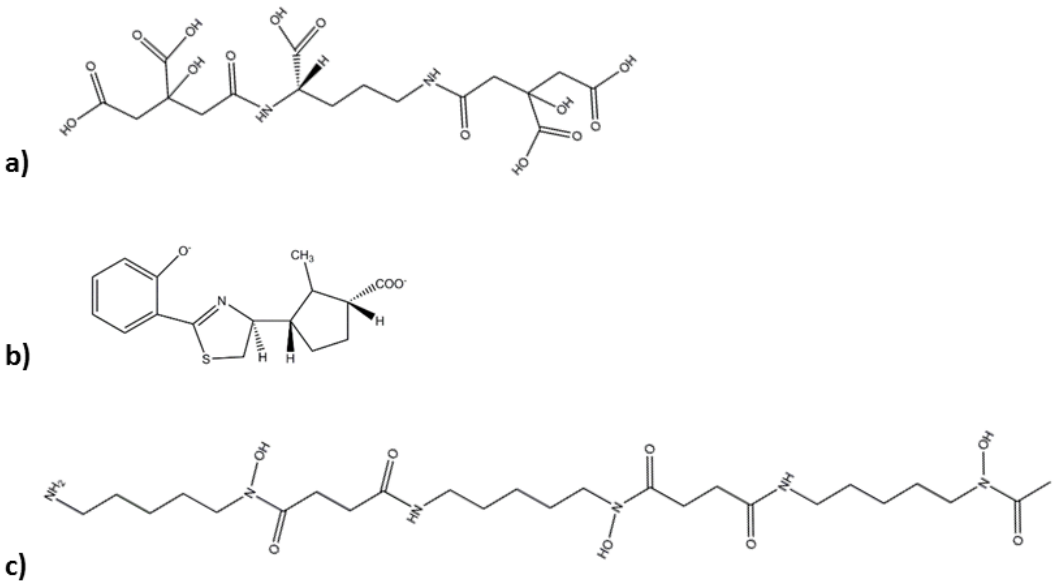

Figure 2-2: Representative siderophore structures: a) staphyloferrin A, b) pyochelin, c) DFO

After complexing Fe^{3+}, the Fe-siderophore complex diffuses in the blood or interstitial fluid until it encounters a bacterium expressing a particular surface receptor to which it can bind. After binding to the surface receptor, the Fe^{3+} in the siderophore is internalized by a strain-specific mechanism. Generalized schema for both Gram-positive and Gram-negative bacteria are shown in *figure 2-3*, below.

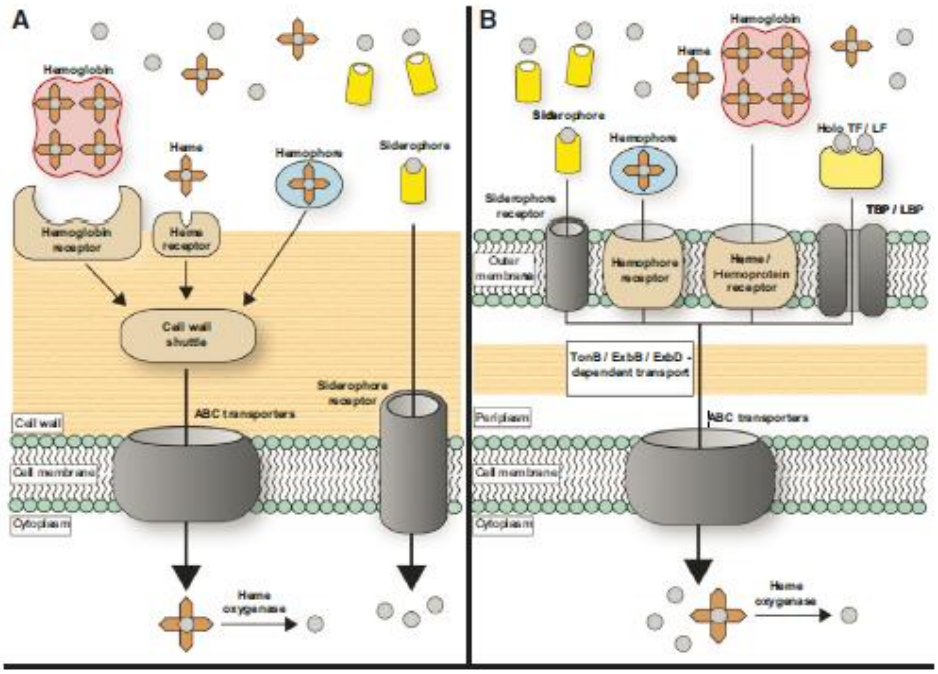

Figure 2-3: Siderophore uptake mechanisms in Gram-positive (left) and Gram-negative (right) bacteria [4]

In bacteria utilizing the siderophore pathway, the siderophores and receptors for the Fe-siderophore complex are constitutively produced in small amounts [4, 6, 9-11, 13]. Lack of iron in their environment de-represses the *Fur* operon, which is responsible for siderophore and receptor production. The bacterium then produces and secretes relatively large quantities of its siderophore(s) [4, 6, 9-11, 13].

2.4.2 Previous Medical Uses of Siderophores

Perhaps the most common use of siderophores is chelation therapy [4, 6, 12], in which siderophores' affinity for Fe^{3+} is exploited to remove Fe^{3+} from the blood. Patients with excessively high blood Fe^{3+} concentrations are given the apo-siderophore desferrioxamine (DFO; *figure 2-4*) intravenously. The apo-DFO complexes any free Fe^{3+} in the blood and is excreted through the kidneys[18, 19] . Patients benefitting from chelation therapy include people with hereditary iron-overload disorders (such as β-thalassemia) [4, 6] and transfusion dependent

patients [20]. Patients given chelation therapy have been shown to have lower infection loads than untreated patients, whose blood iron levels are higher [4, 6].

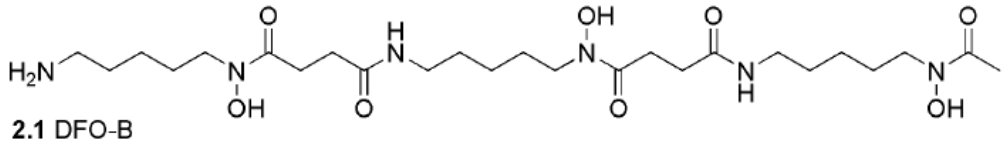

Figure 2-4: DFO-B, used in chelation therapy [17]

Siderophores have the potential to be molecular imaging agents. They bind specifically to their target (particular species of bacteria), they are selectively taken up even at tracer concentrations and they have the capacity to be modified to be tracked via non-invasive methods. These aspects will be further explored in Chapter 3, in which the most effective way to convert siderophores into molecular imaging tracers is examined.

2.5 References

1. Wiley, J., Sherwood, L., and Woolverton, C. *Prescott's Microbiology*. 8th ed. 2011, New York: McGraw-Hill.

2. Davies, J., *Microbes have the last word.* European Molecular Biology Organization Reports, 2007. **8**(7): p. 616-621.

3. Alberts, B. et al, *Molecular Biology of the Cell*. 2002, Garland Science: New York.

4. Cassat, J.E. and Skaar, E.P. *Iron in infection and immunity.* Cell Host Microbe, 2013. **13**(5): p. 509-19.

5. N.N. Greenwood and Earnshaw, A.., *Chemistry of the Elements*. 2nd ed. 2011, Oxford, U.K.: Elsevier.

6. Haley, K.P. and Skaar, E.P., *A battle for iron: host sequestration and Staphylococcus aureus acquisition.* Microbes Infect, 2012. **14**(3): p. 217-27.

7. Earhart, C.F., *Iron Metabolism*, in *The Desk Encyclopedia of Microbiology*. 2009, Elsevier.

8. Beasley, F.C. and Heinrichs, D.E., *Siderophore-mediated iron acquisition in the staphylococci.* J Inorg Biochem, 2010. **104**(3): p. 282-8.

9. Ganz, T., *Iron in innate immunity: starve the invaders.* Curr Opin Immunol, 2009. **21**(1): p. 63-7.

10. Recalcati, S., Locati, M., and Cairo, G., *Systemic and cellular consequences of macrophage control of iron metabolism.* Semin Immunol, 2012. **24**(6): p. 393-8.

11. Johnson, E.E. and Wessling-Resnick, M., *Iron metabolism and the innate immune response to infection.* Microbes Infect, 2012. **14**(3): p. 207-16.

12. Weinberg, E.D., *Iron availability and infection.* Biochim Biophys Acta, 2009. **1790**(7): p. 600-5.

13. Hood, M.I. and Skaar, E.P., *Nutritional immunity: transition metals at the pathogen-host interface.* Nat Rev Microbiol, 2012. **10**(8): p. 525-37.

14. Wooldridge, K.E. and Williams, P.H., *Iron uptake mechanisms of pathogenic bacteria.* FEMS Microbiology Reviews, 1993. **12**: p. 325-248.

15. Chung, M.C.-M., *Structure and Function of Transferrin.* Biochemical Education, 1984. **12**(4): p. 146-154.

16. Wood R.E., et al. *Plasma ATP concentration and venous oxygen content in the forearm during dynamic handgrip exercise.* BMC Physiol, 2009. **24**: p. 6-9.

17. Wencewicz, T.A., *DEVELOPMENT OF MICROBE-SELECTIVE ANTIBACTERIAL AGENTS: FROM SMALL MOLECULES TO SIDEROPHORES*, in *Chemistry*. 2011, University of Notre Dame: South Bend, IN.

18. Pandya, D.N., et al., *Di-macrocyclic terephthalamide ligands as chelators for the PET radionuclide zirconium-89.* Chem Commun (Camb), 2015. **51**: p. 2301.

19. Allain, P., et al., *Pharmacokinetics and renal elimination of desferrioxamine and ferrioxamine in healthy subjects and patients with haemochromatosis.* Br J Clin Pharmacol, 1987. **24**(2): p. 207-12.

20. Elizabeth Abraham, M.D. *Assistant Professor, Division of Nephrology at St. Louis University*. (personal communication).

Chapter 3: Siderophores as Molecular Imaging Agents

When constructing a molecular imaging tracer, it is important to ensure the imaging beacon and targeting moiety are compatible. In the case of PET tracers, one must consider the decay characteristics of the radionuclide, including half-life, β^+ decay fraction, and the energy and type of other decay modes. The chemical behavior of the radionuclide must be such that the tracer atom may be easily and stably incorporated into the tracer without significantly altering the *in vivo* behavior of the tracer [1]. In order to generate images of medical utility, the radionuclide must remain with the tracer until the tracer reaches its target, preferably until the intact tracer is cleared from the body [1].

3.1 Isotopes to Consider

Several radionuclides have characteristics that make them suitable candidates for radiolabeling siderophores. They are all radiometals with chemistry similar to iron, enabling the siderophores to be radiolabeled via a simple complexation reaction. Radiolabeling procedures of this type are simpler, require less technical expertise to perform and reduce radiation dose to personnel compared to the multi-step organic radiosynthetic techniques often used to incorporate radioactive atoms into a molecule's backbone, such as in the radiosynthesis of [^{18}F]FDG [2]. Three radionuclides that could be fruitfully used to radiolabel siderophores are ^{52}Fe, ^{68}Ga and ^{89}Zr.

3.1.1 ^{52}Fe

Because ^{52}Fe ($t_{1/2}$=8.3 h, avg $E_{\beta+}$= 1.9 MeV [3]) is an isotope of iron, it should behave approximately identically to the $^{nat}Fe^{3+}$ that siderophores chelate so selectively[1]. Therefore, ^{52}Fe-siderophore complexes will theoretically be taken up in exactly the same manner and at essentially the same rate as the non-tracer ^{nat}Fe-siderophores. However, because many proteins

in the human body also bind Fe^{3+} and several actually remove Fe^{3+} from Fe-siderophores (e.g., the lipocalins [4]), the presence of ^{52}Fe at a site in the body might not necessarily indicate the presence of ^{52}Fe-siderophores at that site. The observed PET signal could be due to host proteins sequestering ^{52}Fe transchelated from the injected tracer and therefore be of little clinical use, as the signal might not indicate localization of disease. Additionally, this nuclide is produced via the $^{55}Mn(p,4n)^{52}Fe$ reaction [5, 6], which requires a large accelerator to accelerate protons to sufficient energy (~50 MeV) [6]. There are many competing reaction channels and the cross section for production of ^{52}Fe is small. For all these reasons, the use of ^{52}Fe has not been pursued in this work.

3.1.2 ^{68}Ga

Access to ^{68}Ga ($t_{1/2}$= 68 min, avg $E_{\beta+}$=0.846 MeV [7]) is much simpler than ^{52}Fe, since $^{68}Ge/^{68}Ga$ generators are commercially available [8]. These generators typically consist of an ion exchange column to which the parent nuclide (^{68}Ge) is nearly permanently bound [1, 9-11]. When the parent decays to the daughter, the daughter has a much lower affinity for the column material and can be eluted with a suitable solvent. The eluted daughter can then be used for additional radiochemical procedures.[1]. Generators are simple to operate, but they are relatively costly as they must be wholly replaced when the parent material is depleted.

In addition to greater availability, ^{68}Ga has the advantage of having chemistry similar to that of Fe [12, 13]. Molecules that complex Fe^{3+} well (such as transferrin [8]) tend to complex Ga^{3+} readily, so the siderophore imaging literature has focused on ^{68}Ga-labeled siderophores[14-17]. Ga has been shown to have antimicrobial activity [12, 18, 19], so theoretically a ^{68}Ga-siderophore tracer could be used to localize an infection as well as show exactly where a ^{nat}Ga-siderophore (which would specifically deliver cytotoxic doses of the metal to the infection site) would be taken up.

3.1.3 ^{89}Zr

^{89}Zr ($t_{1/2}$=3.3 d, Avg $E_{\beta+}$=0.9 MeV (22.7%) [20]) is an intriguing choice of radiometal for transforming siderophores into PET tracers. While its chemistry is not as close to that of iron as ^{68}Ga, ^{89}Zr does behave very similarly to iron [13] and therefore siderophores will likely complex ^{89}Zr readily. Its half-life is much longer than the biological half-lives of small molecules, but it is likely to form very stable complexes, enabling the activity to be cleared from the body with the tracer, thereby lowering radiation dose to the patient. It can be produced in high specific activity on ordinary biomedical cyclotrons [21], allowing for wider use of the nuclide than ^{52}Fe. However, it emits an additional γ ray (0.91 MeV, 99%)[20] with each decay besides the 511 keV positron peak, giving rise to dosimetry concerns for both patients and personnel.

^{89}Zr was chosen as an initial isotope for use in investigating siderophores as PET tracers, due to its availability, ease of production and novelty as a signal for siderophore imaging.

3.1 Zirconium

3.2.1 Chemistry

Zirconium is a second row transition metal with a chemistry similar to that of iron. Its most common oxidation state is Zr(IV) and it tends to form octavalent (or higher coordinate) complexes [13]. Zr^{4+} is a very hard acidic cation [8] and thus strongly complexes with hard base ligands, particularly those containing N- and O- donors [8, 13]. Many of these complexes, such as Zr-desferrioxamine (Zr-DFO), are kinetically inert to demetallation [22].

The chemical literature for Zirconium focuses on the element's coordination chemistry [23-25], metallurgy (Zr is used as an alloying agent in steel, as well as cladding for fuel in nuclear reactors) [1, 26-28], on zirconium-containing materials for medical devices [29-31], and on zirconium

complexes as components of chromatographic resin for separations of metal ions [32, 33], peptides [34], and small molecules [35].

3.2.2 Biological Role

While the metallurgical and strictly inorganic characteristics of Zr have been heavily investigated (see above), its behavior in living systems has been poorly characterized. The element has no known biological role [36, 37] and transport into any type of cell has never been shown. The adsorption of free Zr to the surface of fungal spores [38], yeast spores [39] and *Citrobacter* [40] has been demonstrated and characterized in bulk. This adsorption has been shown to depend on pH [41, 42]. However, there are no reports of transport of Zr into the cytosol of these potentially infectious cell types. A search of several major databases (PubMed, Web of Science, Science Direct) found only one publication discussing Zr uptake by any sort of infection [43].

3.2.2 Radiochemistry

Since ^{89}Zr decays via positron emission, its location in a system may be ascertained by Positron Emission Tomography (PET). Its fairly low-energy positrons (E_{β}=0.9 (22.7%) and 2.4 (0.2%) MeV [20]) allow high-resolution images to be obtained *in vivo*. However, reports of PET imaging using ^{89}Zr-based tracers have used very large molecular moieties, such as monoclonal antibodies or other large proteins [44]. These tracers are imported into the cell to which they bind. Because ^{89}Zr is biologically inert, it must be attached to these tracers via a suitable bifunctional chelator. The monoclonal antibodies used to target the HER2 receptor [44], Fibroblast activation protein (overexpressed in Rheumatoid arthritis patients) [45], Prostate-specific antigen [32] and other biological targets [44] do not chelate $^{89}Zr^{4+}$ on their own. The chelator most commonly used is 1-(4-Isothiocyanatophenyl)-3-[6,17-dihyroxy-7,10,18,21-tetraoxo-27- [N-acetylhydroxylamino)-6,11,17,22-tetraazaheptaeicosane]thiourea (DFO-NCS), an activated derivative of desferrioxamine (DFO) [32]. DFO is a highly useful chelator: its Zr coordination

chemistry is well-characterized, it completes quantitatively (when in present above tracer concentrations) and the Zr complex is relatively stable in vivo [32]. If DFO is modified by the addition of a benzyl isothiocyanate group, it can be easily conjugated to targeting moieties with free amine groups, such as lysines [32].

3.3 Siderophore Library

The ^{89}Zr complexation efficiency and bacterial uptake behavior of a library of synthetic siderophores were examined. These siderophores were derived from danoxamine (fig. 3-1), a natural product produced by *Streptomyces violaceus* (DSM 8286) [46, 47]. Danoxamine is the iron-binding portion of the salmycin antibiotics these bacteria secrete [47]. While it does not directly have anti-microbial activity, it ensures the specific uptake of salmycin antibiotics by particular microbes.

Members of the library were previously synthesized by systematically modifying the succinyl terminus of danoxamine with a variety of functional groups and variously-sized spacers in order to probe the effect of pKa, stereochemistry, ligand identity and hydrogen bonding ability on the ability of danoxamine to coordinate and complex metal ions [46].

The iron chemistry of the resulting library has already been thoroughly investigated [46, 48]. However, the zirconium chemistry of these compounds and uptake behavior as Zr complexes is unknown.

3.4 Scope of this Work

This work investigates the possibility of using ^{89}Zr-labeled siderophores as molecular imaging agents for infection identification, as well as examining the conditions under which optimal effective specific activity may be obtained for ^{64}Cu.

Because work with radiometals often requires extreme attention to the presence of contaminating metal ions, Chapter 4 presents a thorough investigation of a complexation assay used to determine the effective specific activity of ^{64}Cu and proposes concrete suggestions for obtaining precise, accurate and high ESA values when producing and using this radiometal. Chapter 5 explores the Zr chemistry of a library of danoxamine-derived siderophores and the specificity of their uptake by a variety of bacterial species. Chapter 6 discusses the implications of these results and explores future directions this research could take.

3.5 References

1. Ehmann, W. and Vance. D. *Radiochemistry and Nuclear Methods of Analysis*. Chemical Analysis, ed. J.D. Winefordner. Vol. 116. 1991, New York: John Wiley and Sons. 531.

2. Leung, K., *[18F]Fluoro-2-deoxy-2-D-glucose.* 2005, National Center for Biotechnology Information (US): Bethesda, MD.

3. Junde, H., Su, H., and Chunhui, M. Nuclear Data Sheets, 2007. **108**: p. 773.

4. Weinberg, E.D., *Iron availability and infection.* Biochim Biophys Acta, 2009. **1790**(7): p. 600-5.

5. Qaim, S.M., *Development of novel positron emitters for medical applications: nuclear and radiochemical aspects.* Radiochimica Acta, 2011. **99**(10): p. 611-625.

6. Steyn, G.F., et al., *Production of Fe-52 via proton-induced reactions on manganese and nickel.* Applied Radiation and Isotopes, 1990. **41**(3): p. 315-325.

7. Mccutchan, E.A., Nuclear Data Sheets, 2012. **113**: p. 1735.

8. Wadas, T.J., et al., *Coordinating Radiometals of Copper, Gallium, Indium, Yttrium and Zirconium for PET and SPECT Imaging of Disease.* Chemical reviews, 2010. **110**(5): p. 2858-2902.

9. Ben Azzouna, R., et al., *A new anionic purification method of Ge-68/Ga-68 generator eluate for automated production of Ga-68-peptides.* Journal of Nuclear Medicine, 2015. **56**: p. 1.

10. Cressier, D., et al., *Smoothened titania particles to improve radionuclide separation and their application to the development of a novel Ge-68 / Ga-68 generator.* Rsc Advances, 2015. **5**(37): p. 29319-29324.

11. Le, V.S., et al., *Methods of Increasing the Performance of Radionuclide Generators Used in Nuclear Medicine: Daughter Nuclide Build-Up Optimisation, Elution-Purification-Concentration Integration, and Effective Control of Radionuclidic Purity.* Molecules, 2014. **19**(6): p. 7714-7756.

12. Rangel-Vega, A., et al., *Drug repurposing as an alternative for the treatment of recalcitrant bacterial infections.* Frontiers in Microbiology, 2015. **6**: p. 8.

13. N.N. Greenwood, A.E., *Chemistry of the Elements*. 2nd ed. 2011, Oxford, U.K.: Elsevier.

14. Petrik, M., et al., *Preclinical evaluation of two 68Ga-siderophores as potential radiopharmaceuticals for Aspergillus fumigatus infection imaging.* Eur J Nucl Med Mol Imaging, 2012. **39**(7): p. 1175-83.

15. Petrik, M., et al., *68Ga-siderophores for PET imaging of invasive pulmonary aspergillosis: proof of principle.* J Nucl Med, 2010. **51**(4): p. 639-45.

16. Petrik, M., et al., *68Ga-triacetylfusarinine C and 68Ga-ferrioxamine E for Aspergillus infection imaging: uptake specificity in various microorganisms.* Mol Imaging Biol, 2014. **16**(1): p. 102-8.

17. Mokaleng, B.B., et al., *Synthesis, Ga-68-Radiolabeling, and Preliminary In Vivo Assessment of a Depsipeptide-Derived Compound as a Potential PET/CT Infection Imaging Agent.* Biomed Research International, 2015: p. 12.

18. Zhu, Y.Y., et al., *The Inhibition of Escherichia Coli Biofilm Formation by Gallium Nitrate-Modified Titanium.* Journal of Nanoscience and Nanotechnology, 2015. **15**(8): p. 5605-5609.

19. Sampieri, F., et al., *Efficacy of gallium maltolate against Lawsonia intracellularis infection in a rabbit model.* Journal of Veterinary Pharmacology and Therapeutics, 2014. **37**(6): p. 571-578.

20. Singh, B., Nuclear Data Sheets, 2013. **114**(1).

21. Wooten, A., et al., *Routine Production of 89Zr Using an Automated Module.* Applied Sciences, 2013. **3**(3): p. 593-613.

22. Holland, J.P., Sheh, Y., and Lewis, J. *Standardized methods for the production of high specific-activity zirconium-89.* Nuclear Medicine and Biology, 2009. **36**(7): p. 729-739.

23. Leblanc, M., Maisonneuve,V., and Tressaud, A., *Crystal Chemistry and Selected Physical Properties of Inorganic Fluorides and Oxide-Fluorides.* Chemical Reviews, 2015. **115**(2): p. 1191-1254.

24. Gessner, V., Becker, J., and Feichtner, K., *Carbene Complexes Based on Dilithium Methandiides.* European Journal of Inorganic Chemistry, 2015(11): p. 1841-1859.

25. Zhang, D. and Zi, G., *N-heterocyclic carbene (NHC) complexes of group 4 transition metals.* Chemical Society Reviews, 2015. **44**(7): p. 1898-1921.

26. Baker, T.N., *Role of zirconium in microalloyed steels: a review.* Materials Science and Technology, 2015. **31**(3): p. 265-294.

27. Suman, S., et al., *Hydrogen in Zircaloy: Mechanism and its impacts.* International Journal of Hydrogen Energy, 2015. **40**(17): p. 5976-5994.

28. Guerain, M., et al., *Review of stress fields in Zirconium alloys corrosion scales.* Corrosion Science, 2015. **95**: p. 11-21.

29. Duraccio, D., Mussano, F. and Faga, M., *Biomaterials for dental implants: current and future trends.* Journal of Materials Science, 2015 **50**(14): p. 4779-4812.

30. Saini, M., et al., *Implant biomaterials: A comprehensive review.* World journal of clinical cases, 2015. **3**(1): p. 52-7.

31. Chen, Q.Z. and Thouas, G., *Metallic implant biomaterials.* Materials Science & Engineering R-Reports, 2015. **87**: p. 1-57.

32. Deri, M.A., et al., *PET imaging with 89Zr: From radiochemistry to the clinic.* Nuclear Medicine and Biology, 2013. **40**(1): p. 3-14.

33. Howarth, A.J., et al., *High Efficiency Adsorption and Removal of Selenate and Selenite from Water Using Metal-Organic Frameworks.* J Am Chem Soc, 2015.

34. Wang, Z.G., et al., *Development of the Affinity Materials for Phosphorylated Proteins/Peptides Enrichment in Phosphoproteomics Analysis.* Acs Applied Materials & Interfaces, 2015. **7**(16): p. 8377-8392.

35. Li, Y., et al., *Development and comparison of two multi-residue methods for the analysis of select pesticides in honey bees, pollen, and wax by gas chromatography-quadrupole mass spectrometry.* Talanta, 2015. **140**: p. 81-7.

36. Ghosh, S., Sharma, A., and Talukder, G., *Zirconium. An Abnormal Trace Element in Biology.* Biological Trace Element Research, 1992. **35**: p. 247-271.

37. Lloyd, J.R. and Renshaw, J. , *Microbial transformations of radionuclides: fundamental mechanisms and biogeochemical implications*, in *Metal Ions in Biological Systems*. 2005.

38. Bhatti, H.N. and Amin, M., *Removal of zirconium(IV) from aqueous solution by Coriolus versicolor: Equilibrium and thermodynamic study.* Ecological Engineering, 2013. **51**: p. 178-180.

39. Akhtar, K., Ahktar, M.W., and Khalid, A. M., *Removal and recovery of zirconium from its aqueous solution by Candida tropicalis.* Journal of Hazardous Materials, 2008. **156**: p. 108-117.

40. Basnakova, G., and Macaskie, L., *Accumulation of zirconium and nickel by Citrobacter sp.* Journal of Chemical Technology and Biotechnology, 1999. **74**: p. 509-514.

41. Garnham, G., Codd, G., and Gadd, G., *Accumulation of zirconium by microalgae and cyanobacteria.* Applied Microbiology and Biotechnology, 1993. **39**(4-5): p. 666-672.

42. Dhami, P.S., et al., *Biosorption of radionuclides by Rhizopus arrhizus.* Biotechnology Letters, 1998. **20**(3): p. 225-228.

43. Severin, G.W., et al., *The impact of weakly bound 89Zr on preclinical studies: Non-specific accumulation in solid tumors and aspergillus infection.* Nuclear Medicine and Biology, 2014.

44. Lamberts, L.E., et al., *Antibody Positron Emission Tomography Imaging in Anticancer Drug Development.* Journal of Clinical Oncology, 2015. **33**(13): p. 1491-1503.

45. Laverman, P., et al., *Immuno-PET and Immuno-SPECT of Rheumatoid Arthritis with Radiolabeled Anti-Fibroblast Activation Protein Antibody Correlates with Severity of Arthritis.* Journal of Nuclear Medicine, 2015. **56**(5): p. 778-783.

46. Wencewicz, T.A., *DEVELOPMENT OF MICROBE-SELECTIVE ANTIBACTERIAL AGENTS: FROM SMALL MOLECULES TO SIDEROPHORES*, in *Chemistry*. 2011, University of Notre Dame: South Bend, IN.

47. Vértesy, L., Aretz, W., Fehlhaber, H., Koger, H., *Salmycin A-D, Antibiotika aus Streptomycese violaceus, DSM 8286, mit Siderophore-Aminoglycosid-Struktur.* Helv. Chim. Acta 1995. **78**: p. 46-60.

48. Wencewicz, T.A., et al., *Trihydroxamate siderophore-fluoroquinolone conjugates are selective sideromycin antibiotics that target Staphylococcus aureus.* Bioconjug Chem, 2013. **24**(3): p. 473-86.

Chapter 4: Sources of metal contamination and specific activity measurement variations in cyclotron produced ^{64}Cu

NB: This work is currently out for review at *Applied Radiation and Isotopes* as "Sources of metal contamination and specific activity measurement variations in cyclotron produced ^{64}Cu" Nora C. Goscinski, Tara Mastren, Paul Eisenbeis, Efrem Mebrahtu, Suzanne E. Lapi.

High effective specific activity (ESA) of ^{64}Cu is important for high-efficiency radiolabeling with this radiometal, but the sources of metal contaminants that can interfere with radiolabeling are not fully known. Additionally, accurate determination of this parameter is important for determining batch purity and the TETA titration, a common method for finding ^{64}Cu ESA, has not been fully characterized. The purpose of this study was twofold, firstly to identify sources of metal contaminants in the ^{64}Cu production process and secondly to identify metals that interfere with the binding of ^{64}Cu to the TETA chelator. Possible sources of contamination at all stages of the ^{64}Cu production process were identified. The Cu^{2+}-TETA complexation reaction was characterized for repeatability and interferences, and the interfering metal profiles of a variety of reaction vessels and reagents were quantified. Our results indicate that the TETA titration method for determining ^{64}Cu ESA has both relative standard deviations of 27.6% and 40.3% for repeatability and reproducibility respectively and the chelator TETA is selective for picomolar amounts of Cu^{2+} in the presence of low millimolar concentrations of Zn^{2+} and Ni^{2+}.

4.1 Introduction

4.1.1 ^{64}Cu Specific Activity and Sources of Contamination

The positron-emitting metal ^{64}Cu is emerging as an important radionuclide for Positron Emission Tomography (PET) and has been incorporated into radiopharmaceuticals for imaging a variety of targets such as hypoxia [1-3], amyloid-β plaques [4,5] and numerous targets on cancer cells [6-9]. Producing this isotope in high specific activity is important for efficient radiolabeling and for the production of high specific activity radiopharmaceuticals for imaging of low abundance targets. Additionally, accurately determining the effective specific activity (ESA, radioactivity per μmol of competing metal ions) of ^{64}Cu is necessary as the presence of other metals in ^{64}Cu may decrease the radiochemical yield of a radiolabeling procedure. However, in selecting a method for determining the ESA of a radiometal, it is important to consider the chemistry of the final radiolabeling procedure. A quality control assay that is less selective than the chemistry to be performed will give a falsely-low ESA value for the radiometal, while a QC procedure that is far more selective could return a high ESA value that underestimates the effects of interfering species in the final radiolabeling reaction.

Cold metal contaminants may enter cyclotron-produced ^{64}Cu at many points during the production process. Reagents used to prepare the ^{64}Ni target may contain non-Ni metal atoms. Trace amounts of dissolved metals in target cooling water could be deposited on the target backing and inadvertently mixed with ^{64}Cu during target processing. Additionally, the reagents and resin used for post-bombardment processing may not be metal-free, and incomplete separation of ^{64}Cu and ^{64}Ni may occur. Trace amounts of cold metals could leach from the containers into which ^{64}Cu is dispensed and stored. The reagents and vessels used for the TETA titration itself may contain sufficient levels of extractable cold metals to interfere with

complexation of Cu by the chelator. Finally, sample manipulation during target transfer, dispensing and the TETA titration requires exposure to potential airborne metals.

4.1.2 ESA Determination

There are many methods of determining ESA of ^{64}Cu, including ion chromatography [10], liquid chromatography-mass spectrometry [11] and titration of Cu^{2+} with a selective chelator, most typically 1,4,8,11-tetraazacyclotetradecane-1,4,8, 11-tetraacetic acid (TETA) [10, 12, 13]. TETA is considered selective for Cu^{2+} because the binding constant (log K value) for Cu^{2+}-TETA (log K=21.7) [14,15] is larger than the log K values for Ni^{2+}-TETA (19.9) [14,15], or Zn^{2+}-TETA (log K=16.4) [14,15]. (All log K values refer to the $M + L \leftrightarrow ML$ equilibrium, where L is the completely deprotonated chelator.) The TETA titration method is a popular method for determining ^{64}Cu ESA, but the assay itself has never been fully characterized as a method. Additionally, while the effect of metal ions on the formation of other complexes, such as ^{68}Ga-DOTA [16-18], ^{68}Ga-NOTA [17-18] and ^{68}Ga-DTPA [18] has been thoroughly examined, no such analysis has been done for the formation of ^{64}Cu-TETA in the presence of other metal ions.

4.1.3 Sources of Error

The goal of characterizing an assay is to determine the reliability of the results it returns. Some of the aspects typically examined include the assay's repeatability (precision when the same sample is analyzed multiple times by a single analyst), reproducibility (precision when the same sample is analyzed by different analysts), and robustness (precision and accuracy in the presence of chemical contaminants or slight variations in experimental conditions), including the method's selectivity for the analyte in the presence of similar substances [19].

Potential sources of error in the TETA titration method of determining ^{64}Cu ESA include a chelator that is either more or less selective than the chelator used in radiolabeling, a protocol

that is inherently low-throughput and vulnerable to human error, and the presence of other metals in the reaction from a variety of sources.

All of the above sources of metal contamination and error in the ^{64}Cu-TETA complexation method were examined. The TETA titration was independently performed by two analysts for 17 batches of ^{64}Cu. The extractable metal content for a variety of vessel types and reagents was profiled and quantified. The effects of Ni^{2+} and Zn^{2+} on Cu^{2+}-TETA complexation were examined by spiking in the cold metals at a variety of concentrations and comparing the resulting ESA to the ESA of pure (as received) ^{64}Cu. Additionally, the repeatability and reproducibility of the TETA titration results were examined and the metal content of the materials used in ^{64}Cu production and final ^{64}Cu production batches were profiled and quantified by ion chromatography.

4.2 Materials and Methods

4.2.1 Materials

All chemicals were trace-metal grade and used as received unless otherwise noted. In-house milliQ water (18 MΩ-cm) was used to prepare solutions unless otherwise noted. 1,4,8,11-tetraazacyclotetradecane-1,4,8, 11-tetraacetic acid (TETA) was purchased from Macrocyclics (Dallas, TX).

Ammonium acetate, ammonium sulfate, methanol (reagent grade), TraceSelect Ultra water, TraceCERT atomic absorption spectroscopy standards (1000 mg/L Fe^{3+}, Cu^{2+}, Ni^{2+}, Zn^{2+} ,Co^{2+} in nitric acid), and ethylenediaminetetraacetic acid (EDTA) were purchased from Sigma Aldrich (St. Louis, MO). Glass-backed silica thin layer chromatography plates (silica gel 60 F-254) were purchased from EMD Millipore (Billerica, MA). Nitric acid, 96-well plates (polystyrene),

screwcap microcentrifuge tubes (virgin polypropylene, polypropylene screwcap with O-ring), snaptop microcentrifuge tubes (high clarity polypropylene, DNase/RNase-free, pyrogen-free), 5 mL Polyvials for ASDV autosampler with plain caps, and 15 and 50 mL conical centrifuge tubes (polypropylene, non-pyrogenic), were obtained from Fisher Scientific (Waltham, MA). Polystyrene 96-well plates were also purchased from Santa Cruz Biotechnology (Santa Cruz, CA). Ethanol (absolute) was purchased from DeCon Labs (King of Prussia, PA). Concentrated PDCA eluent (35 mM pyridine-2,6-dicarboxylic acid, 330 mM KOH, 28 mM K_2SO_4, 370 mM formic acid), solid 4-(2-pyridylazo)resorcinol (PAR), and PAR diluent (1.0 M 2-dimethylaminoethanol, 0.50 M NH_4OH, 0.30 M $NaHCO_3$) were purchased from Dionex (Sunnyvale, CA) and diluted to working concentrations with milliQ water and PAR diluent, respectively. 5 mL (6 mL) Norm-Ject Luer-Lock syringes (polypropylene, pyrogen-free, sterile) were purchased from Henke-Sass-Wolf (Tuttlingen, Germany) and used as received for manual injections for ion chromatography. Target cooling water was sampled from the CS-15 cyclotron and stored in polypropylene syringes before analysis. ^{64}Cu (as $^{64}CuCl_2$) was produced in-house using an automated module [21]. Concentrated sulfuric acid (99.9999% metals basis) and NH_4OH (99.99% metals basis) were purchased from Alfa Aesar (Ward Hill, MA).

4.2.2 Instrumentation

A high performance liquid chromatography unit consisting of a Dionex ICS-3000 HPLC with a 1 mL sample loop, a GP50 pump, an AD20 absorbance detector, an AS-DV autosampler and a column heater (Thermo Scientific) was used for ion chromatography analysis. An IonPac CS5A analytical column was used with an IonPac CG5A guard column (Dionex) to separate metals extracted from vessels and reagents. The post-column reagent PAR (0.06 g/L) was delivered using pressurized helium via a PC10 pneumatic controller (Dionex). For manual injections, the

sample was injected onto the column using a 5 mL Norm-Ject syringe. When the AS-DV autosampler was used to deliver sample to the column, EDTA- and acid-washed polyvials were used. A CRC-25R dose calibrator (Capintec, Ramsey NJ) was used for all activity measurements. TLC plates were analyzed for activity with a RadioTLC plate reader (Bioscan, Washington DC).

4.2.3 Acid Washing

Strict acid-washing protocols were followed to ensure that reaction and storage vessels had minimal extractable metal contents. Unless otherwise noted, vessels for use in the TETA titration were acid washed as follows: complete immersion in 1:1 concentrated nitric acid: milliQ H_2O for ≥4 hours followed by a rinse with absolute ethanol. They were then dried overnight in an oven (37^0C). The acid-washed vessels were closed and stored in screw-top jars (subjected to the same acid-washing protocol) until use. The polyvials used by the ASDV autosampler required a more rigorous metal-extraction procedure before use: the vials and caps were rinsed with milliQ H_2O, soaked in 1 M EDTA (alkalinized with solid NaOH until all EDTA dissolved) for at least 48 hours and again rinsed with milliQ H_2O before immersion in a 1:1 HNO_3:H_2O bath (described above) for a minimum of 48 hours. The autosampler vials and caps were stored in the acid bath until use, when they were rinsed with milliQ H_2O before being filled with sample. In an attempt to reduce sample contamination, ion chromatography samples were prepared immediately before analysis.

4.2.4 TETA Titration

The TETA titration was performed as previously described[12, 13]. Briefly, 7.4 MBq (200 µCi, 20 µL) ^{64}Cu were added to a series of vials or wells in a 96-well plate containing 8 different concentrations of TETA (in 0.1 M NH_4OAc buffer, pH 5.5) and enough 0.1 M NH_4OAc to bring

the volume to 80 µL. The solutions were placed on a shaking incubator and incubated for 60 minutes at 80 ^{0}C. The percent ^{64}Cu complexation was determined via radioTLC: 1 µL aliquots from each solution were spotted on TLC plates and developed in 1:1 MeOH: 10% NH_4OAc (pH 5.5). Developed plates were placed on a RadioTLC plate reader for analysis. For interference analysis, 40 µL Ni^{2+} or Zn^{2+} was added to the reaction before ^{64}Cu; the volume of 0.1 M NH_4OAc was reduced accordingly.

4.2.5 Metal Profiles

Samples were prepared by heating 0.1 M NH_4OAc at 80 ^{0}C for 1 hour (as per the TETA titration protocol) in a variety of reaction vessels. The heated NH_4OAc was then diluted (1:200) with milliQ water (for autosampler runs) or UltraTrace water (for manual injections). The samples were separated and quantified as previously described [10]. Briefly, a 1 mL injection loop was used to load samples onto the analytical column, PDCA eluent was pumped through the column at 0.3 mL/minute and a post-column mixing loop was used to mix metals eluting from the column with 4-(2-pyridylazo)resorcinol, which complexed metal ions in effluent. The concentration of the metal-PAR complex was monitored via UV at 530 nm.

4.2.6 Analysis

Data were analyzed using Prism (Graphpad, CA). Selectivity coefficients were calculated using an arbitrary low number of mols of Cu ($1x10^{-12}$ mols) for comparison, as the concentration of Cu^{2+} ions in received ^{64}Cu was typically below the detection limit of ion chromatography.

4.3 Results

4.3.1 Reproducibility and Repeatability

For the 17 ^{64}Cu production batches tested, the difference between ESA values obtained by different analysts was significant (P=0.0196 for Analyst 1 vs Analyst 2). ESA values determined

using TETA titration obtained by a single analyst for a single batch of ^{64}Cu was variable and ranged from 0.9 % to 27.6%. (Analyst 2 error bars, *figure 4-1).*

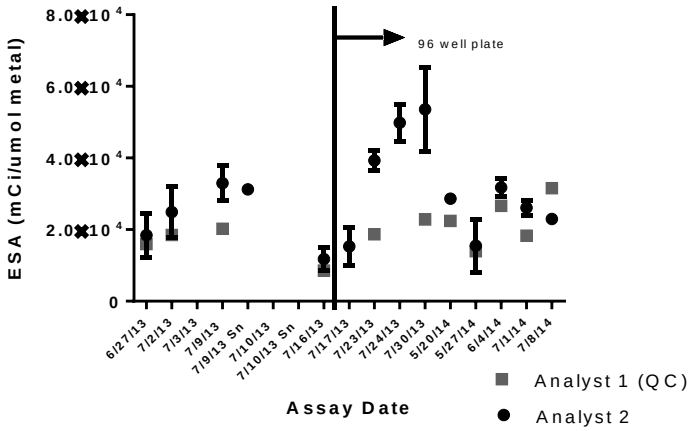

Figure 4-1: Effective specific activity of ^{64}Cu as determined by complexation with TETA. ESA's before 7/17/13 were determined using acid-washed polypropylene vials. ESAs on or after 7/17/13 were determined using polystyrene 96 well plates.

The ESA of ^{64}Cu increases with batch size (R=0.390) and this effect is statistically significant. However, batch size does not seem to affect the precision of the TETA assay, as the correlation between batch size and the standard error of the mean is not statistically significant. The variation in Cu-TETA complexation behavior (seen in the size of the standard error of the mean ESA) is likely inherent to the complexation reaction itself, because more-precise ESA values are not obtained for production batches with higher concentrations of ^{64}Cu.

4.3.2 Selectivity of TETA for Cu^{2+}

To verify the selectivity of TETA for Cu^{2+} in the presence of large excesses of other divalent first-row transition metal ions, Zn^{2+} and Ni^{2+} were spiked into the TETA titration at a variety of concentrations, the effect on ^{64}Cu ESA was determined, and the selectivity coefficients of TETA for Cu^{2+} in the presence of the contaminants were calculated. A value of $K_{\text{analyte interferent}}$ between

+1 and -1 indicates that the method is more selective for the analyte than the interferent [19]. When the interferences of Zn^{2+} and Ni^{2+} with Cu^{2+}-TETA complexation were examined, $K_{Cu, Zn}$ was found to be $8.34x10^{-4}$ while $K_{Cu. Ni}$ was $4.62x10^{-3}$, indicating that while TETA is highly selective for Cu^{2+}, Ni^{2+} is more likely to interfere with Cu^{2+} complexation than Zn^{2+}.

Ni^{2+} was spiked into the Cu-TETA complexation reaction to achieve final Ni^{2+} concentrations ranging from 1.7 to 204 µM (*figure 4-2*; for clarity, only the lowest spike concentrations are shown). As expected, the presence of Ni^{2+} lowered the ESA of ^{64}Cu. When the difference in ESA caused by the spike was normalized to the unspiked ^{64}Cu ESA, the interference increased linearly with Ni^{2+} concentration. At spike concentrations below 2.25 µM, ESA variation can no longer be ascribed to the presence of spiked-in Ni^{2+}, as the error bars for Ni^{2+}-spiked and unspiked ^{64}Cu ESA's overlap below this concentration.

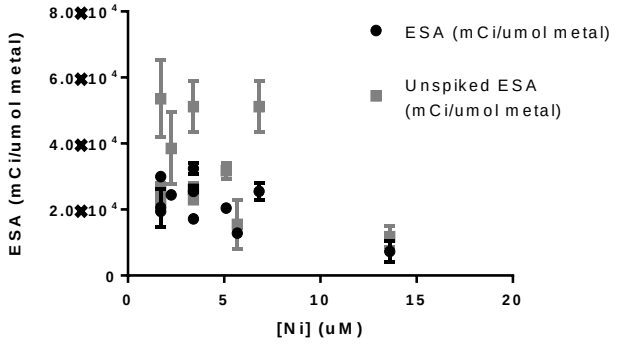

Figure 4-2: Effect of Ni^{2+} spike on ^{64}Cu ESA

Zn^{2+} interference was determined by spiking Cu-TETA complexation reaction at a variety of concentrations, from 2.75 to 183.5 µM (*figure 4-3*). The presence of Zn^{2+} lowered the ESA of ^{64}Cu at all but the lowest concentration tested (2.75 µM, *figure 4-3)*. At spike concentrations below 5.1 µM, the error bars for spiked and unspiked ^{64}Cu-TETA complexation reactions overlap; therefore, Zn^{2+} is no longer the sole cause of ESA variation below 5.1 µM.

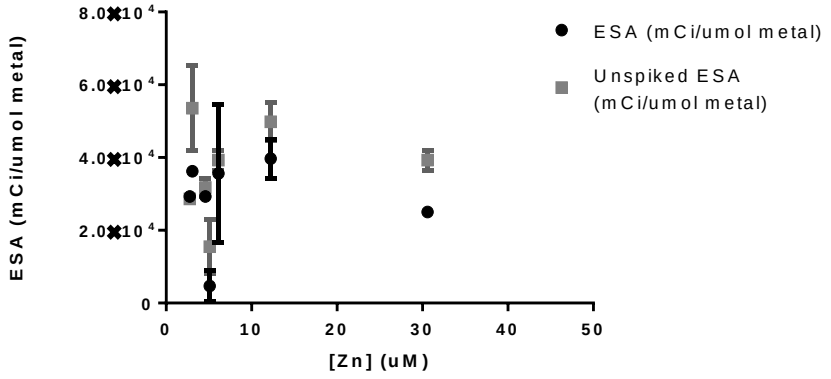

Figure 4-3: Effect of Zn^{2+} spike on ^{64}Cu ESA

4.3.3 Sources of Interference: Metal content of vessels, reagents and ^{64}Cu

Labeling buffer (0.1 M NH_4OAc) was heated in a variety of reaction vessels made of different types of plastic to determine extractable metal content. The vessels were incubated as received and after acid-washing. The metal content of the labeling buffer after incubation was determined via ion chromatography. Unheated labeling buffer and other reagents were also analyzed.

The labeling buffer was essentially metal free when prepared with milliQ water, with the exception of Zn^{2+}, which is present at levels below those found in all reaction vessels (*table 4-1*). Polystyrene 96-well plates (as received) have the lowest extractable metal levels of all vessels tested.

Acid-washing increased the Zn^{2+} content of molecular biology grade (DNase/RNase-free) snaptop tubes nearly 9x, despite the use of trace metal grade HNO_3. Trace metal grade HNO_3 was found to contain approximately 7 µM Zn^{2+} (*table 4-1)*, suggesting that direct transfer of Zn^{2+} from the acid bath to tubes is unlikely. It is possible the acid had time to loosen but not completely liberate Zn^{2+} from the polypropylene matrix. However, acid washing appears to lower the levels of extractable Cu^{2+} and Zn^{2+} in polypropylene screwtop tubes, suggesting that different grades of polypropylene contain different concentrations of Zn^{2+}.

Table 4-1: Metal concentrations (μM) in TETA reaction mixture due to leaching from reaction vessel

Metal	0.1 M NH_4OAc (pH 5.5)	HNO_3	96 well plate (as received)	Screwtop vials (as received)	Screwtop Vials (acid-washed)	'premium' Snaptop Vials* (as received)	'premium' Snaptop Vials* (acid washed)
Fe^{3+}	< blank	< blank	< blank	< blank	< blank	<blank	<quant limit
Cu^{2+}	< blank	0.37	0.75	0.43	< blank	0.72	0.82
Ni^{2+}	< blank	< blank	< blank	<blank	< blank	<blank	<quant limit
Zn^{2+}	0.38	7.20	0.55	68.35	11.37	7.31	67.91
Co^{2+}	Not detected	<blank	Not detected	<blank	< quant limit	Not detected	<quant limit
[TETA] (well 5, ~EC_{50})	0.15	0.15	0.15	0.15	0.15	0.15	0.15
Plastic Type	---	--	Polystyrene	Polypropylene	Polypropylene	High clarity Polypropylene	High clarity Polypropylene

*'Premium' vials were molecular biology grade.

Quantification of the metal profiles of ^{64}Cu production batches after decay found no significant correlation between total metal content and ESA (*figure 4-4)*. Additionally, cold metals were found to be present at millimolar concentrations (*table 4-2*) while the TETA titration indicates that Cu^{2+} is present at picomolar concentrations in CuOAc, so TETA is still highly selective for Cu^{2+}.

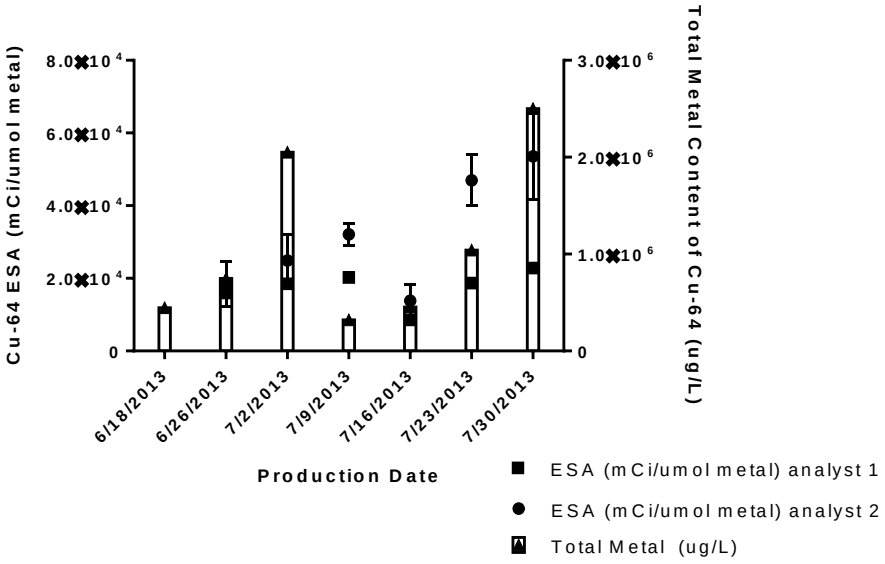

Figure 4-4: Effect of total metal content on precision of ^{64}Cu ESA

Table 4-2: Metal profiles of selected ^{64}Cu production batches

Metal (μM)	6/18/2013	6/26/2013	7/2/2013	7/9/2013	7/16/2013	7/23/2013	7/30/2013
Fe^{3+}	1085	--	--	--	--	--	--
Cu^{2+}	--	--	--	--	16	--	--
Ni^{2+}	2096	2794	2488	5486	1874	11416	5435
Zn^{2+}	4023	8932	29214	--	5231	5583	33344
Co^{2+}	--	--	--	--	--	--	--

4.3.4 Sources of interference: Metal content of cyclotron target cooling water and separation reagents

It has been noted [13] that target cooling water can be a source of cold metal contaminants in cyclotron-produced ^{64}Cu. Therefore, the metal content of cyclotron target cooling water was examined via ion chromatography over several ^{64}Cu productions. The total metal content of the target cooling water tracks with ^{64}Cu ESA—higher ESA is seen for batches with high metal concentrations in the cooling water and a major drop in ESA is seen when metal content of cooling water drops (due to water change-out; *figure 4-5*). However, the exact cause of this relationship remains undetermined.

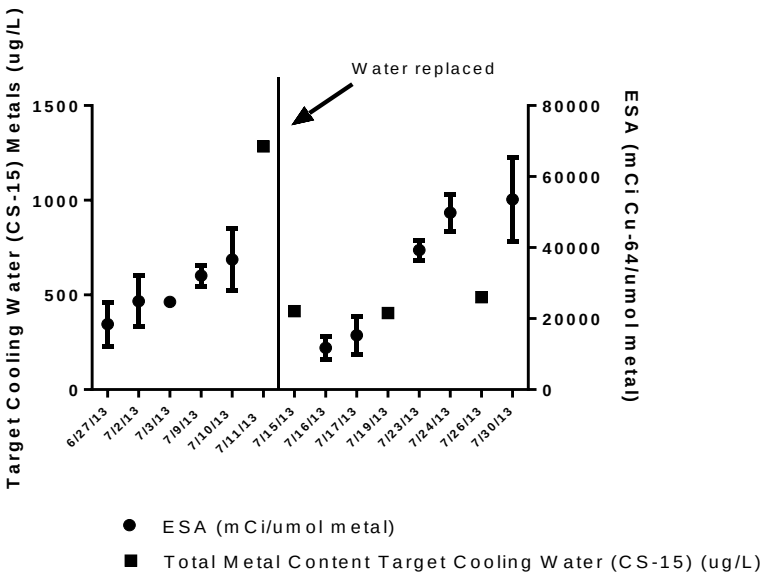

Figure 4-5: Effect of CS-15 target cooling water metal content on ^{64}Cu ESA

The resin and acid solutions used in target processing were also analyzed for metal content via ion chromatography (*table 4-3)*. When treated with 6 M HCl, unused AG1-X8 anion exchange resin was found to have high levels of extractable Zn^{2+} (5604 μg/L) and Fe^{3+} (4136 μg/L), with smaller amounts of Cu^{2+} and Ni^{2+}. 0.5 M HCl, used to elute purified ^{64}Cu during target processing, had similarly high concentrations of Fe^{3+} and Zn^{2+}. However, after passage through a column of AG1-X8 resin, the 0.5 M HCl had no detectable Fe^{3+} and the Zn^{2+} content doubled to 10,959 μg/L. The Ni content of the 0.5 M HCl increased from 744 μg/L to 1674 μg/L after passing through the resin, while the Cu^{2+} content remained fairly constant (1546 μg/L pre-, 1414 μg/L post-column) This suggests that AG1-X8 resin binds Zn^{2+} at high concentrations of HCl, but freely releases the metal when treated with 0.5 M HCl . Thus, the resin used to separate ^{64}Cu from the ^{64}Ni target may be a major contributor to the cold metal contaminants found in cyclotron-produced ^{64}Cu.

Table 4-3: Metal profiles of reagents used in ^{64}Cu separation

Metal (µg/L)	0.5 M HCl		6 M HCl passed through fresh resin
	Pre-column	Post-column	
Fe^{3+}	3930	--	4136
Cu^{2+}	1546	1414	1546
Ni^{2+}	744	1674	589
Zn^{2+}	5943	10959	5604

All the reagents used to prepare ^{64}Ni targets contained Fe^{3+} (up to 2.87 mg/mL), while $(NH_4)_2SO_4$ also contained Ni^{2+} (1.59 mg/mL) and NH_4OH contained Cu^{2+} (2.04 mg/L). Cobalt was not detected in any target processing reagents.

4.4 Discussion

When comparing ESA values for a single batch of ^{64}Cu obtained by different analysts, the standard error of the mean ranged from 5.1% to 40.3% of the mean ESA, while the standard error for ESA values obtained by a single analyst ranged from 0.9% to 27.6% of the mean. The repeatability and reproducibility of the assay appear to be batch dependent. This may be due to the extremely low analyte concentration, as typical concentrations of ^{64}Cu are in the picomolar range. At such low concentrations, it may take a long time for the chelator and metal ion to form a complex and even tiny differences in reaction mixture composition or conditions can dramatically affect the kinetics of the complexation process. Likely the thermodynamic product ($^{64}Cu^{2+}$-TETA) is formed after a long incubation at high temperature, but perhaps 60 minutes at 80^0C does not provide sufficient thermal energy to minimize the formation of kinetic products such as Ni^{2+}-TETA or Zn^{2+}-TETA. Additionally, reaction pH may affect the affinity of a

chelator for various metal ions. TETA was chosen for its high affinity for Cu^{2+} in its completely deprotonated form, but at pH 5.5, other, more-protonated forms of TETA may exist, each with its own set of stability constants.

There is a positive correlation between ^{64}Cu batch size and ESA of the ^{64}Cu (R= 0.390). A possible explanation for the increase in specific activity with increasing amounts of ^{64}Cu produced is that the number of moles of cold interferents is essentially constant from batch to batch, since they are inherent to the production process. Producing more activity would then lead to higher ESA values, since the number of ^{64}Cu atoms increases compared to the constant number of interferent atoms.

The Cu^{2+}-TETA complexation reaction is perturbed by high concentrations of other metals in the reaction mixture. The mean ESA of ^{64}Cu spiked with contaminant metals is lower (2.3-69.7% lower) than the unspiked ESA for all production batches assayed. The macrocycle TETA does complex Cu^{2+} with high selectivity, as indicated by complete complexation of ^{64}Cu (approximately picomolar) by only picomoles of TETA in the presence of micromoles of cold Ni^{2+} and Zn^{2+}, as well as by selectivity coefficient (for Cu^{2+}) values much less than one. However, the vast excess of cold Ni^{2+} and Zn^{2+} ions in the reaction vessel likely leads to their complexation by TETA, giving rise to lower ESA values for ^{64}Cu.

Cold Ni^{2+} and Zn^{2+} in the ^{64}Cu come from a number of sources. Incomplete recovery of the ^{64}Ni target material is likely a source of cold Ni^{2+} which is present as the main contaminant. Cold Zn^{2+} found in AG1-X8 resin itself may co-elute with ^{64}Cu during target processing.

Alternatively, the resin may concentrate cold Zn^{2+} from the target, plastics and solvents, then release it in the same fraction as ^{64}Cu. Additionally, many common plastic vessels contain significant amounts of extractable, interfering metal ions even after acid-washing. Polystyrene was found to have the lowest amount of extractable metals, though polypropylene could also be nearly metal-free. The initial TETA titration assay was performed in virgin polypropylene vials containing large quantities of extractable metals, and the ESA values obtained with these vials are consistently lower than those obtained in other vessels. The use of polystyrene 96 well plates to run the TETA complexation reaction gave consistently higher ESA values for ^{64}Cu than polypropylene vials and is inherently higher-throughput.

In order to obtain more accurate ESA values for batches of ^{64}Cu, we recommend running the TETA assay multiple times in parallel in polystyrene 96-well plates, using extremely high-purity metal-free reagents. AG1-X8 resin used to separate ^{64}Cu from ^{64}Ni should be washed with 0.5 M HCl before use to remove cold metal ions. If non-molecular-biology grade polypropylene is used to run the TETA assay or to store ^{64}Cu, the vessels should be thoroughly soaked in trace-metal grade acid to remove extractable metals from the plastic before use. Careful manipulation of samples and vessels, with constant attention to the possibility of metal contamination, is also necessary to obtain high ESA and realistic ESA values and for subsequent high specific activity radiochemistry.

4.5 Conclusion

The Cu^{2+}-TETA complexation assay has been characterized as a standard method. It is perturbed by the presence of other first-row transition metal ions in the reaction mixture. Ni^{2+} interferes with Cu-TETA complexation at spike concentrations below 2.25 µM, while Zn^{2+}

interferes with the assay at spike concentrations below 5.1 µM. Sources of interfering metals include Ni^{2+} and other metal ions from the target, ion exchange resin used in target processing, and reaction vessel material with polystyrene and molecular biology grade polypropylene having the smallest amounts of extractable metal ions.

4.6 References

1. Handley, M.G., et al., *Cardiac hypoxia imaging: second-generation analogues of 64Cu-ATSM.* J Nucl Med, 2014. **55**(3): p. 488-94.

2. Handley, M.G., et al., *PET imaging of cardiac hypoxia: opportunities and challenges.* J Mol Cell Cardiol, 2011. **51**(5): p. 640-50.

3. Zeglis, B.M., et al., *Underscoring the influence of inorganic chemistry on nuclear imaging with radiometals.* Inorg Chem, 2014. **53**(4): p. 1880-99.

4. Hickey, J.L. and Donnelly, P.S., *Diagnostic imaging of Alzheimer's disease with copper and technetium complexes.* Coordination Chemistry Reviews, 2012. **256**(19-20): p. 2367-2380.

5. Hickey, J.L., et al., *Diagnostic imaging agents for Alzheimer's disease: copper radiopharmaceuticals that target Abeta plaques.* J Am Chem Soc, 2013. **135**(43): p. 16120-32.

6. Tavare, R., et al., *Enhanced immunoPET of ALCAM-positive colorectal carcinoma using site-specific 64Cu-DOTA conjugation.* Protein Eng Des Sel, 2014.

7. Viola-Villegas, N.T., et al., *Understanding the pharmacological properties of a metabolic PET tracer in prostate cancer.* Proceedings of the National Academy of Sciences of the United States of America, 2014. **111**(20): p. 7254-7259.

8. Zhou, Y., Baidoo, K.E., and Brechbiel, M.W., *Mapping biological behaviors by application of longer-lived positron emitting radionuclides.* Adv Drug Deliv Rev, 2013. **65**(8): p. 1098-111.

9. Marquez, B.V., et al., *Development of a Radio labeled Irreversible Peptide Ligand for PET Imaging of Vascular Endothelial Growth Factor.* Journal of Nuclear Medicine, 2014. **55**(6): p. 1029-1034.

10. Mastren, T., et al., *Specific activity measurement of (6)(4)Cu: a comparison of methods.* Appl Radiat Isot, 2014. **90**: p. 117-21.

11. Zeng, D. and Anderson, C.J., *Rapid and sensitive LC-MS approach to quantify non-radioactive transition metal impurities in metal radionuclides.* Chem Commun (Camb), 2013. **49**(26): p. 2697-9.

12. Kume, M., et al., *A semi-automated system for the routine production of copper-64.* Appl Radiat Isot, 2012. **70**(8): p. 1803-6.

13. McCarthy, D.W., et al., *Efficient production of high specific activity Cu-64 using a biomedical cyclotron.* Nuclear Medicine and Biology, 1997. **24**(1): p. 35-43.

14. Anderegg, G., et al., *Critical evaluation of stability constants of metal complexes of complexones for biomedical and environmental applications* (IUPAC Technical Report).* Pure and Applied Chemistry, 2005. **77**(8).

15. Chaves, S., Delgado, R., and Da Silva, J.J.R.F., *The stability of the metal complexes of cyclic tetra-aza tetra-acetic acids.* Talanta, 1992. **39**(3): p. 249-254.

16. Oehlke, E., et al., *Influence of metal ions on the (6)(8)Ga-labeling of DOTATATE.* Appl Radiat Isot, 2013. **82**: p. 232-8.

17. Simecek, J., et al., *How is (68)Ga labeling of macrocyclic chelators influenced by metal ion contaminants in (68)Ge/(68)Ga generator eluates?* ChemMedChem, 2013. **8**(1): p. 95-103.

18. Chakravarty, R., et al., *Detailed evaluation on the effect of metal ion impurities on complexation of generator eluted 68Ga with different bifunctional chelators.* Nucl Med Biol, 2013. **40**(2): p. 197-205.

19. Harvey, D., *Modern Analytical Chemistry*. 1st ed. 2000, Boston: McGraw-Hill.

Chapter 5: ^{89}Zr-siderophores as molecular imaging agents for bacterial infections

Siderophores are small molecules synthesized by bacteria to harvest Fe^{3+} from their environment. In infection scenarios, their production can increase infection virulence. Their selective uptake *in vivo* in multi-bacteria environments indicates that this class of molecules has the potential to be selective imaging agents. In this study, DFO-NCS and a library of trihydroxamate siderophores were evaluated as vehicles to deliver ^{89}Zr selectively to bacteria for Positron Emission Tomography (PET) imaging of infections. The uptake of ^{89}Zr-DFO-NCS by human cells (SKBR3), *Staphylococcus aureus*, and *Pseudomonas aeruginosa* was significantly different ($p<0.0001$) and highest for *S. aureus*. The Zr chemistry and bacterial uptake behavior of a library of trihydroxamate siderophores was evaluated and compared to that of DFO-NCS. Uptake of ^{89}Zr-DFO-NCS and another siderophore library member (^{89}Zr-V-129) were tested in a murine lung infection model (*P. aeruginosa*, PA M57-15) and ^{89}Zr-V-129 was found to have significantly higher lung uptake in infected mice ($p=0.0120$) than in control mice. The uptake of ^{89}Zr-DFO-NCS did not differ significantly between control and infected mice ($p=0.831$). ^{89}Zr-siderophores have the potential to be selective, specific PET tracers for imaging bacterial infections *in vivo* and should be explored more thoroughly.

5.1 Introduction

Zirconium-89 is an emerging radiometal that has been successfully used to image a variety of diseases *in vivo*. As discussed in section 3.2.1, ^{89}Zr is biologically inert and must be attached to

molecular imaging tracers via a suitable bifunctional chelator. The chelator most commonly used is 1-(4-Isothiocyanatophenyl)-3-[6,17-dihyroxy-7,10,18,21-tetraoxo-27- [N-acetylhydroxylamino)-6,11,17,22-tetraazaheptaeicosane]thiourea (DFO-NCS), an activated derivative of desferrioxamine (DFO) [1]. DFO is a highly useful chelator: its Zr coordination chemistry is well-characterized ,the reaction completes quantitatively (when in excess) and the Zr complex is relatively stable in vivo [1]. If DFO is modified by the addition of a benzyl isothiocyanate group, it can be easily conjugated to targeting moieties with free amine groups, such as lysines [1].

However, ^{89}Zr-DFO alone has the potential to target certain diseases, such as bacterial infections, as a small-molecule complex. One area of current interest in the infection imaging community is the development of siderophore-based PET tracers.

Because siderophores chelate Fe^{3+} so avidly, they can be radiolabeled with radiometals whose chemistry resembles that of Fe^{3+}. In fact, DFO is a siderophore, originally produced by *Streptomyces pilosus* [2, 3] and used clinically to lower the blood concentration of Fe^{3+} in patients with hereditary iron-overload disorders (such as β-thalassemia) [4, 5] and transfusion dependent patients [6] in addition to its use as a ^{89}Zr chelator. While the literature has previously focused on^{68}Ga-labeled siderophores [7-10], ^{89}Zr could also be used to transform a siderophore into an infection-targeted PET tracer. While its chemistry is not as close to that of iron as ^{68}Ga, ^{89}Zr does behave very similarly to iron [11] and therefore siderophores with similar structures to DFO will likely complex ^{89}Zr readily. These ^{89}Zr-siderophore complexes are likely to be quite kinetically stable, enabling the activity to be cleared from the body with the tracer, thereby

lowering patient radiation dose. ^{89}Zr can be produced in high specific activity on a biomedical cyclotron equipped with a solid target station [12], allowing for widespread use. Despite the many advantages ^{89}Zr has to offer the PET chemist, it has been neglected in the arena of infection imaging. A search of several major databases (PubMed, Web of Science, Science Direct) found only one publication discussing Zr uptake by any sort of infection [13].

We present herein the first report of using ^{89}Zr to image bacterial infections. ^{89}Zr-DFO-NCS was characterized as a tracer for bacterial infections. The ^{89}Zr chemistry of a library of siderophores based upon DFO was explored (see *figure 5-1* for selected structures): the complexation efficiency and stability towards demetallation of the ^{89}Zr-siderophore complexes was examined and the complexes' uptake by a panel of Gram-positive and Gram-negative bacteria was determined. Finally, the efficacy of ^{89}Zr-siderophores as tracers for imaging bacterial infections *in vivo* was tested by examining the uptake of ^{89}Zr-DFO-NCS and the ^{89}Zr complex of one siderophore (V-129) by *Pseudomonas aeruginosa* (PA M57-15) in a murine lung infection model.

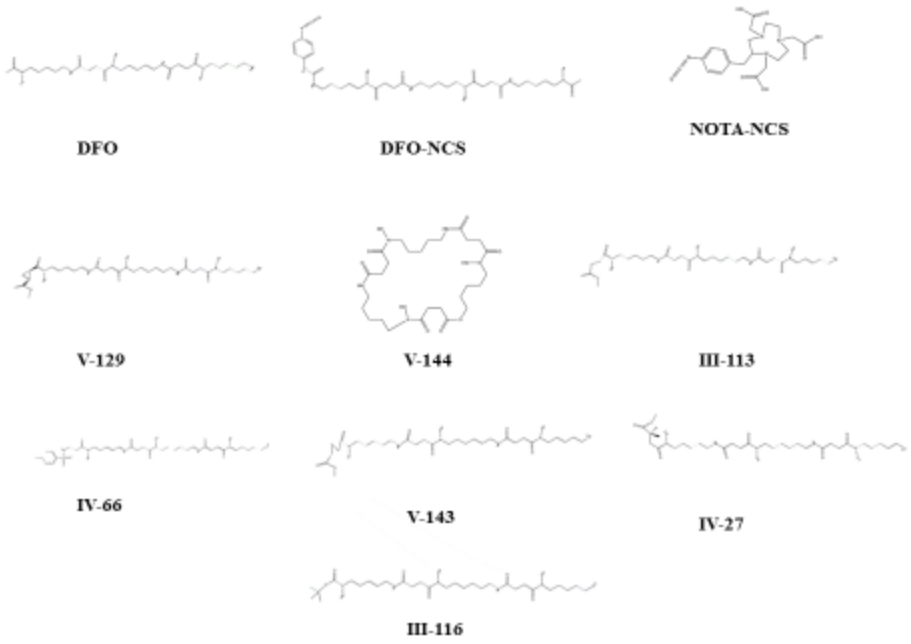

Figure 5-1: Selected chelators used in this study

5.2 Materials and Methods

5.2.1 Materials

All chemicals were reagent grade unless otherwise noted. In-house milliQ water (18 MΩ) was used to prepare solutions unless otherwise noted. 1-(4-Isothiocyanatophenyl)-3-[6,17-dihyroxy-7,10,18,21-tetraoxo-27-[N-acetylhydroxylamino)-6,11,17,22-tetraazaheptaeicosane]thiourea (DFO-NCS) was purchased from Macrocyclics, Inc (Dallas, TX). HCl and NaOH were purchased from Fisher Scientific (Waltham, MA). *S. aureus* (ATCC 11632) was provided by Dr. Tim Wencewicz (Washington University, St. Louis), while *Pseudomonas aeruginosa* cultures were provided by Dr. Steven Brody (Washington University, St. Louis). SKBR3 cells were obtained from ATCC. An incubator, culture tubes, inoculation loops and petri dishes were obtained from Fisher Scientific (Waltham, MA). Agar was purchased from Lambda Biotech

(Ballwin, MO). LB (Miller) powdered media, diethylenetriaminepentaacetic acid (DTPA), Deferoxamine mesylate (DFO), and 4-(2-Hydroxyethyl)piperazine-1-ethanesulfonic acid (HEPES) were obtained from Sigma Aldrich (St. Louis, MO). Mannitol salt agar (MSA) was obtained from VWR International (Radnor, PA). 70% ethanol was prepared using 200 proof ethanol (in-house) and milliQ (18 MΩ-cm) H_2O. ^{89}Zr was produced in-house using an automated module [12] and was received as ^{89}Zr-oxalate.

5.2.2 ^{89}Zr Radiochemistry

^{89}Zr was neutralized in HEPES buffer (0.5 M, pH 7.1) and pH adjusted to 6.8-7.1 with NaOH and/or HCl. Solid DFO-NCS was dissolved in DMSO (4-7 mg/mL) and diluted to 0.1 mg/mL in HEPES. DFO-NCS and neutralized ^{89}Zr were mixed to obtain an M:L ratio of 1:5, then incubated on a shaker (Eppendorf thermomixer, Fisher Scientific) at 37 ^{0}C for 60 minutes. The extent of ^{89}Zr chelation was determined by TLC. Briefly, 5 μL 50 mM DTPA (in milliQ H_2O) were added to an aliquot of the ^{89}Zr-DFO-NCS complexation mixture and incubated at 37 ^{0}C 5 minutes further before spotting on chromatography paper (CHR, Whatman, Pittsburgh, PA). The strips were developed in 50 mM DTPA and analyzed for activity with a RadioTLC plate reader (Bioscan, Washington DC). Likewise, siderophore library members were dissolved in water (1-2 mg/mL), then diluted in HEPES buffer (0.5 M, pH 7.1) to a working concentration of 0.1 mg/mL. The siderophore working solution and neutralized ^{89}Zr were then mixed (M:L ~1:5) and incubated on a shaker at 37 ^{0}C. For bacterial uptake studies, the siderophores were allowed to complex with ^{89}Zr for 60 minutes. For stability studies, aliquots were removed at various times and spotted on chromatography paper as above. The TLC strips were developed and visualized as above.

5.2.3 Biological Assays

Staphylococcus aureus and *Pseudomonas aeruginosa* were grown in a stationary incubator (37 ^{0}C) for 18-24 hours in LB (Miller) broth. 500 µL aliquots of the cultures were incubated at 37 ^{0}C with neutralized ^{89}Zr or ^{89}Zr-DFO-NCS (5 minutes, unless otherwise noted). The cells were then centrifuged and washed twice with saline (0.9% NaCl) to remove non-specifically bound ^{89}Zr. Pellet activity was then quantified with a dose calibrator (CRC-25R, Capintec, Ramsey NJ). The incubation time, cell concentration, ^{89}Zr/^{89}Zr-DFO-NCS dose and concentration of Fe^{3+}-depleting compounds in the media were all varied. Internalization was determined by sonicating cell pellets (resuspended in sterile saline) for 5 minutes, followed by centrifugation. The activity present in cytosol (supernatant) and membrane (pellet) fractions was then measured.

5.2.4 *In vivo* Studies

A clinical isolate of P. aeruginosa designated PA M57-15 ($1X10^5$ CFU/30ul) was intra-trachealy instilled into mice (CD-1 white male, 6-8 weeks of age) one hour prior to imaging. 20 µg siderophore (V-129 or DFO-NCS) were incubated with 1 mCi ^{89}Zr in HEPES (0.5 M, pH 7.1) at 37°C for 1 hour, then diluted in saline. 70 – 90 µCi of the radiotracer was then injected into mice intratracheally instilled either with PA M57-15 bacteria in PBS or PBS only (negative control). Dynamic imaging was done for 0 – 40 min, followed by static imaging at 3 h post-injection. At 18 hours post-delivery of PA M57-15, the mice were euthanized for biodistribution studies.

5.3 Results and Discussion

5.3.1 ^{89}Zr-DFO as baseline siderophore: *in vitro* studies

In order to determine whether chelation affects ^{89}Zr uptake by bacterial cells, cultures of *S. aureus* were treated with free ^{89}Zr (neutralized, but not otherwise manipulated) and with ^{89}Zr-DFO-NCS (90-130 µCi/tube). After 5 minutes' incubation at 37^0, the cultures were centrifuged and the activity present in each wash fraction, as well as the initial supernatant and final pellet,

was quantified. The vast majority of ^{89}Zr remained in the media in both cases, but when chelated with DFO-NCS, up to 24.2% of ^{89}Zr was found associated with *S. aureus* cells (*figure 5-2a*). (Note that the percentages of free ^{89}Zr do not add up to 100%. The difference was retained by pipet tips.) Promisingly, unchelated ^{89}Zr did not bind to or enter the bacterial cells at all. Because 'free' ^{89}Zr is not taken up by bacterial cells, any ^{89}Zr uptake observed *in vivo* will be from an intact ^{89}Zr-siderophore, rather than a 'lost' ion of ^{89}Zr.

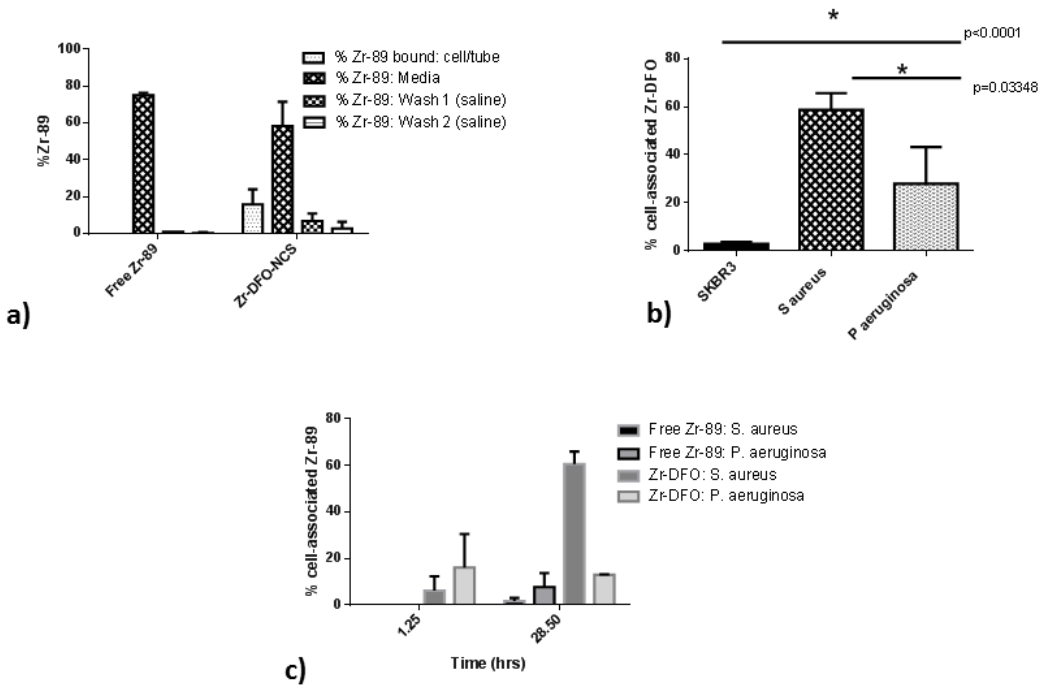

Figure 5-2: a) Effect of chelation on binding of ^{89}Zr to *S. aureus* cells; b) selectivity of ^{89}Zr-DFO-NCS uptake by mammalian cells, Gram-Positive bacteria (*S. aureus)* and Gram-negative bacteria (*P. aeruginosa*); and c) time-dependence of ^{89}Zr and ^{89}Zr-DFO-NCS uptake by Gram-positive and Gram-negative bacteria

The selectivity of ^{89}Zr-DFO-NCS uptake was investigated by incubating model Gram-positive (*S. aureus*) and Gram-negative (*P. aeruginosa*) bacteria, as well as human cells (SKBR3), with ^{89}Zr-DFO-NCS as above. *S. aureus* bound the highest fraction of ^{89}Zr-DFO-NCS (58.8 ±6.9%), with *P. aeruginosa* binding significantly less (28.0±15.3%) and the mammalian cells binding

nearly none (3.0±0.7%) of the applied complex (*figure 5-2b*). The extreme disparity between the fraction of ^{89}Zr-DFO-NCS bound by bacterial cells and mammalian cells indicates that the complex may have the ability to selectively bind to/be taken up by bacterial cells in the presence of mammalian cells, such as in the context of an infection. It also raises the possibility that ^{89}Zr-DFO-NCS may be a tracer well-suited to imaging bacterial infections *in vivo*, as there would be very little off-target (non-infection) uptake. Additionally, the twofold higher uptake ($p=0.0335$) of ^{89}Zr-DFO-NCS by *S. aureus* than by *P. aeruginosa* indicates that the complex is selectively taken up by Gram-positive bacteria. This selectivity suggests the possibility of developing more-targeted tracers (based on DFO-NCS) for identification of bacterial infections.

To examine the effect of incubation length on ^{89}Zr-DFO-NCS uptake by the two types of bacteria, cultures of both *S. aureus* and *P. aeruginosa* were treated with 5-10 μCi ^{89}Zr (neutralized oxalate complex) or ^{89}Zr-DFO-NCS and incubated at 37^0C (stationary) for approximately 30 hours. While no uptake of free radiometal by either strain of bacteria was seen at 60 minutes, by 28 hours post-labeling both *S. aureus* and *P. aeruginosa* showed slight uptake of free ^{89}Zr (*S.* aureus: 1.7±1.3%, *P. aeruginosa* 7.7±6.0%). As expected, uptake of ^{89}Zr-DFO-NCS was much higher than that of the free radiometal at both 90 minutes and 29 hours (*figure 5-2c*). Interestingly, at 90 minutes, *P. aeruginosa* had much higher cell-associated activity (16.1±14.4% vs 6.2±6.1% for *S. aureus*), whereas after 29 hours, *S. aureus* once more bound the majority of the complex. Because very short (5-10 min) and very long (29 h) incubation periods result in higher selectivity of ^{89}Zr-DFO-NCS for *S. aureus* than intermediate time points, the temporal aspect of bacterial uptake experiments with this complex should be carefully planned.

When the uptake behaviors of unfunctionalized DFO and DFO-NCS were compared, only the activated chelator was taken up (*figure 5-3*), while uptake of unfunctionalized DFO was negligible. While this could indicate that DFO-NCS binds covalently to free amine groups on cellular surfaces, the specificity of its uptake suggests that the story is more complex. When the uptake of ^{64}Cu-NOTA-NCS by the panel of bacteria was examined, all of the strains tested took up a negligible amount of the NOTA-NCS complex. Because ^{64}Cu-NOTA-NCS is essentially not taken up while ^{89}Zr-DFO-NCS is avidly taken up, the role of NCS in siderophore uptake is likely more complex than simply serving to covalently anchor the siderophore complex to the outer bacterial membrane.

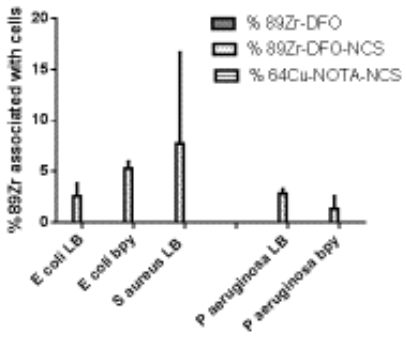

Figure 5-3: Effect of p-Bn-SCN group on uptake of ^{89}Zr-DFO by S. aureus, P aeruginosa and E coli.

5.3.2 Behavior of Siderophore Library

Of the siderophores examined, only ^{89}Zr-III-116, ^{89}Zr-IV-27, ^{89}Zr-V-144, ^{89}Zr-V-129 and ^{89}Zr-V-143 were taken up by any of the bacteria tested (*figure 5-4a-b*). While ^{89}Zr-DFO-NCS was taken up to varying extents by all bacteria tested (*figure 5-4a*), ^{89}Zr-V-144 was only taken up by Fe^{3+}-deprived *S. aureus* ($p<0.0001$), indicating that ^{89}Zr-V-144 may select for Gram-positive organisms under infection-like conditions (*figure 5-4b*). Iron-starved *E. coli* took up over 10x

more ^{89}Zr-V-143 than Fe^{3+}-deprived *S. aureus* (p=0.00057), indicating that ^{89}Zr-V-143 may select for Gram-negative organisms. ^{89}Zr-siderophore uptake is specific to bacterial type, growth conditions and the siderophore itself, indicating that finding a siderophore avidly taken up by a given bacterium may require testing a large library of compounds.

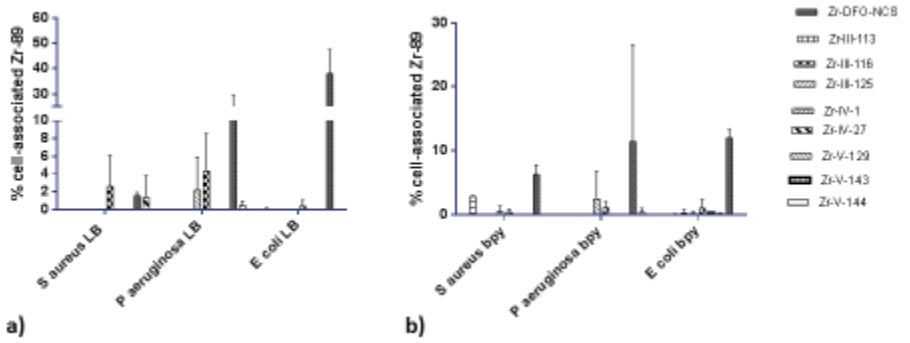

Figure 5-4: Uptake of ^{89}Zr-siderophore complexes by Gram-positive and Gram-negative bacteria grown under a) iron-replete conditions, b) iron-deficient conditions.

5.3.3 *In vivo* Studies

When ^{89}Zr-DFO-NCS and ^{89}Zr-V-129 were administered to mice with *P. aeruginosa* lung infections, different clearance routes were observed for ^{89}Zr-V-129 and ^{89}Zr-DFO-NCS. ^{89}Zr-DFO-NCS cleared through the kidneys as expected [14, 15] , while the ^{89}Zr-V-129 complex undergoing hepatobiliary clearance (*figure 5-5c*). When the lung uptake of infected and control (uninfected) mice was examined, the uptake of ^{89}Zr-V-129 was significantly higher (p=0.012) in infected mice at early timepoints (12.5-32.5 minutes; *figure 5-5a*). For ^{89}Zr-DFO-NCS, the difference in lung uptake between infected and control mice was not significant (p=0.83; *figure 5-5b*). At the extended timepoint of the biodistribution study (>17 h post-injection), the lung uptake of neither tracer was significantly different between infected and healthy mice (*figure 5-*

5d). However, the difference in lung uptake seen 12.5-32.5 minutes post-injection for ^{89}Zr-V-129 is promising and shows that ^{89}Zr-siderophores could be used as tracers for infection imaging. Structural optimization is likely required to find a siderophore/bacteria combination with enhanced uptake differences *in vivo*. Further studies are warranted to determine the optimal siderophore structures for PET imaging of various types of infections.

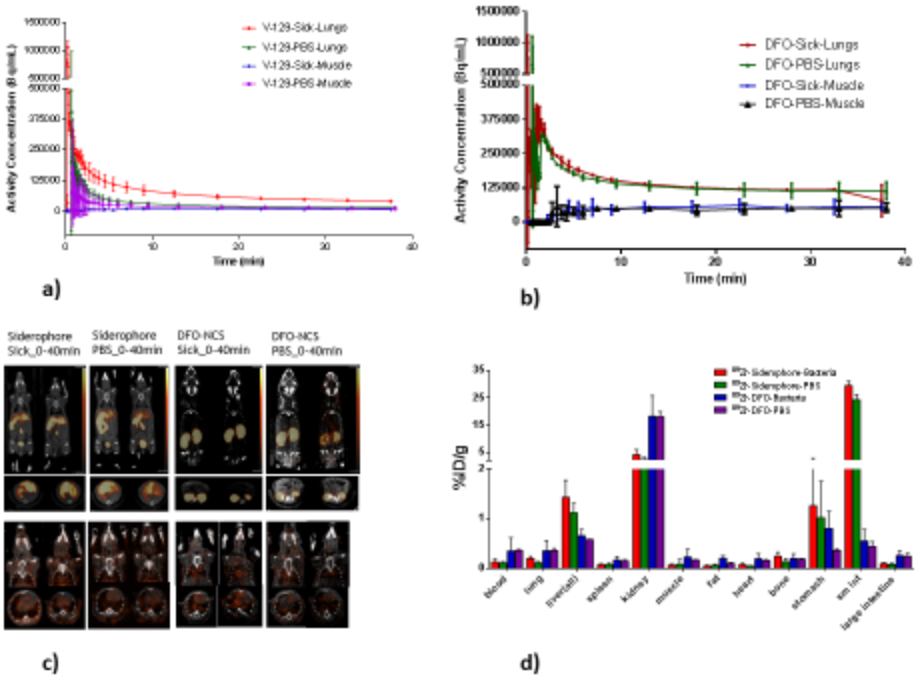

Figure 5-5: : a) time-activity curve for ^{89}Zr-V-129 *in vivo*; b) time-activity curve for ^{89}Zr-DFO-NCS *in vivo;* c) *in vivo* uptake of ^{89}Zr-DFO-NCS and ^{89}Zr-V-129 (static scan, 3 hr post-injection); d) biodistribution of ^{89}Zr-DFO-NCS and ^{89}Zr-V-129 in mice (sacrificed 17 h post-injection)

5.4 Conclusion

The complex ^{89}Zr-DFO-NCS has been validated as a radiotracer for bacteria. The complex is selective for Gram-positive bacteria, but can be taken up slightly by the Gram-negative *Pseudomonas aeruginosa*. Siderophores based on DFO are also selectively taken up by bacterial cells *in vitro* and *in vivo* and therefore have the potential to be novel PET tracers when chelating ^{89}Zr.

5.5 References

1. Deri, M.A., et al., *PET imaging with 89Zr: From radiochemistry to the clinic.* Nuclear Medicine and Biology, 2013. **40**(1): p. 3-14.

2. Davis, B.A. and Porter, J.B., *Results of Long Term Iron Chelation Treatment With Deferoxamine*, in *Iron Chelation Therapy*, C. Hershko, Editor. 2002, Kluwer Academic/Plenum Press: New York. p. 91-126.

3. Kalinowski, D. and Richardson, D.R., *The Evolution of Iron Chelators for the Treatment of Iron Overload Disease and Cancer.* Pharmacological Reviews, 2005. **57**(4): p. 547-583.

4. Cassat, J.E. and Skaar, E.P *Iron in infection and immunity.* Cell Host Microbe, 2013. **13**(5): p. 509-19.

5. Haley, K.P. and Skaar, E.P *A battle for iron: host sequestration and Staphylococcus aureus acquisition.* Microbes Infect, 2012. **14**(3): p. 217-27.

6. Elizabeth Abraham, M.D. *Assistant Professor, Division of Nephrology at St. Louis University*, Personal communication.

7. Petrik, M., et al., *Preclinical evaluation of two 68Ga-siderophores as potential radiopharmaceuticals for Aspergillus fumigatus infection imaging.* Eur J Nucl Med Mol Imaging, 2012. **39**(7): p. 1175-83.

8. Petrik, M., et al., *68Ga-siderophores for PET imaging of invasive pulmonary aspergillosis: proof of principle.* J Nucl Med, 2010. **51**(4): p. 639-45.

9. Petrik, M., et al., *68Ga-triacetylfusarinine C and 68Ga-ferrioxamine E for Aspergillus infection imaging: uptake specificity in various microorganisms.* Mol Imaging Biol, 2014. **16**(1): p. 102-8.

10. Mokaleng, B.B., et al., *Synthesis, Ga-68-Radiolabeling, and Preliminary In Vivo Assessment of a Depsipeptide-Derived Compound as a Potential PET/CT Infection Imaging Agent.* Biomed Research International, 2015: p. 12.

11. Greenwood, N.N. and Earnshaw, E., *Chemistry of the Elements*. 2nd ed. 2011, Oxford, U.K.: Elsevier.

12. Wooten, A., et al., *Routine Production of 89Zr Using an Automated Module.* Applied Sciences, 2013. **3**(3): p. 593-613.

13. Severin, G.W., et al., *The impact of weakly bound 89Zr on preclinical studies: Non-specific accumulation in solid tumors and aspergillus infection.* Nuclear Medicine and Biology, 2014.

14. Pandya, D., Pailloux, S., Tatum, D., Magda, D., Wadas, T.J., *Di-macrocyclic terephthalamide ligands as chelators for the PET radionuclide zirconium-89.* Chem Commun (Camb), 2015. **51**: p. 2301.

15. Allain, P., et al., *Pharmacokinetics and renal elimination of desferrioxamine and ferrioxamine in healthy subjects and patients with haemochromatosis.* Br J Clin Pharmacol, 1987. **24**(2): p. 207-12.

5.6 Supplementary Information

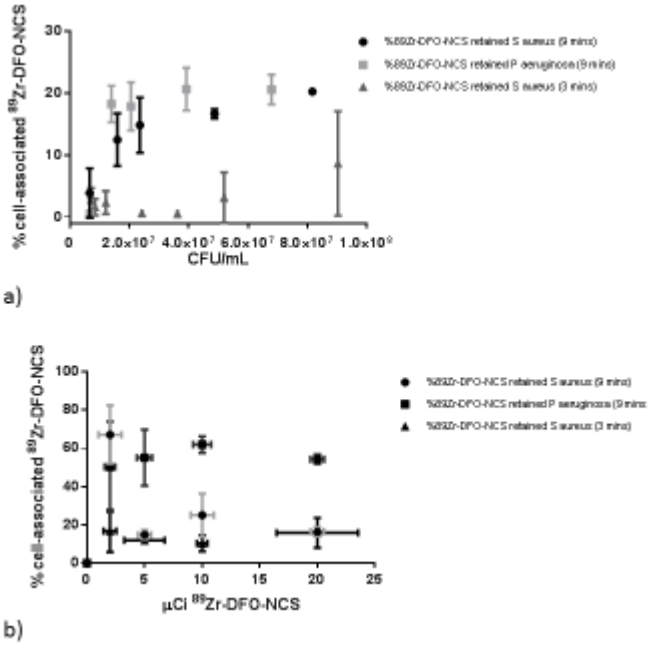

Figure 5-6: a) effect of varying cell (*S. aureus* and *P. aeruginosa*) concentration on uptake of 10 µCi ^{89}Zr-DFO - NCS; b) effect of varying ^{89}Zr-DFO-NCS dose on tracer uptake by *S. aureus* and *P. aeruginosa*

Neat cultures of *S. aureus* and *P. aeruginosa* were spiked with 0 to 30 µCi ^{89}Zr-DFO-NCS in order to study the effect of dose on tracer fraction bound. The highest fraction of ^{89}Zr-DFO-NCS was found to stick when 5-10 µCi were administered to 500 µL culture. However, the total amount of activity bound to each cell pellet was so small in this range that internalization studies could not be performed with a dose calibrator. Consequently, 20 µCi/500 µL culture was selected as the standard dose.

Chapter 6: Concluding Remarks

Radionuclides have the potential to reveal reams of information about living systems, information that cannot be easily obtained via other techniques. In particular, nuclei that emit positrons can be incorporated into molecules in order to track the movement of the molecule within a living system via PET imaging. Radiometals have the potential to probe systems which move too slowly for the shorter-lived organic radioisotopes (^{18}F, ^{11}C) as well as systems in which the movement of a particular metal is of interest. However, before a radiometal-radiotracer combination can be fruitfully used to investigate biological questions, the radiochemistry of the nuclide itself as well as the radiotracer as a whole must be thoroughly understood.

6.1 Efficacy of TETA Titration at Determining Effective Specific Activity of ^{64}Cu

The Cu^{2+}-TETA complexation assay has been characterized as a standard method. It is perturbed by the presence of other first-row transition metal ions in the reaction mixture. Ni^{2+} interferes with Cu-TETA complexation at spike concentrations below 2.25 μM, while Zn^{2+} interferes with the assay at spike concentrations below 5.1 μM. Sources of interfering metals include Ni^{2+} and other metal ions from the target, ion exchange resin used in target processing, and reaction vessel material with polystyrene and molecular biology grade polypropylene having the smallest amounts of extractable metal ions.

Thoroughly understanding the intimate details of assays used to determine effective specific activity of radiometals and other radionuclides is necessary for these materials to be used

rationally. While the TETA titration assay is a useful tool for rapid determination of the quality of a ^{64}Cu batch, it is conducted on tracer-concentration material and therefore the presence of contaminants several orders of concentration above the analyte will perturb the assay. However, these contaminants will also affect the radiolabeling chemistry performed by the final user of the ^{64}Cu. Therefore, care should be taken to eliminate or minimize the presence of contaminating metal ions in production reagents and materials, storage vessels and containers for radiolabeling when working with radiometals, particularly ^{64}Cu.

6.2 Viability of ^{89}Zr-siderophores as Tracers for PET Imaging of Bacterial Infections

DFO-NCS, a well-established chelator for ^{89}Zr, has been characterized as a targeting moiety in itself when complexing ^{89}Zr. ^{89}Zr-desferrixoamine and other ^{89}Zr-radiolabled trihydroxamate siderophore chelators have been shown to target bacterial cells *in vitro*. While their activity towards bacteria when complexed with Fe^{3+} is well-characterized, these compounds retain their affinity for bacteria when complexed with $^{89}Zr^{4+}$. Compounds in a small library of siderophores were examined for stability of ^{89}Zr chelation and affinity for various Gram-positive and Gram-negative bacteria. Uptake specificity of these compounds varied: ^{89}Zr-DFO-NCS was taken up to varying extents by all bacteria tested, while some ^{89}Zr-siderophore complexes were not taken up by any of the strains, by only a fraction of the species or only when the bacteria were deprived of Fe^{3+}. The variations in uptake behavior indicate that ^{89}Zr-siderophores have the potential to be tracers that specifically identify living bacterial cells.

In vivo studies validated *in vitro* results. ^{89}Zr-siderophores can be selectively taken up by bacterial infection *in vivo* and tracer uptake is not seen in uninfected animals. While the results

are not dramatic, tracer uptake in the area of infection (lung) was significantly higher in infected than in control mice. However, this increased uptake was only true for one of the two tracers tested, indicating that a given strain of bacteria will potentially only take up certain ^{89}Zr-siderophores. Additional investigations in this area could lead to the identification of tracer-bacterial pairs giving clinicians a powerful tool to confirm diagnoses, monitor infection dynamics and determine appropriate courses of treatment for individual patients.

6.3 Future Directions

^{89}Zr-siderophores could be used in the future as radiotracers to image bacterial infections *in vivo* via PET. However, these tracers must be thoroughly investigated in order to find the optimal tracer to use for a given infection type before human imaging studies can begin. In the course of this future investigation, methods will need to be validated, models confirmed and results verified. The development of ^{89}Zr-siderophores as PET tracers for bacterial infections promises to be an interesting and fruitful endeavor with implications for personalized medicine.

For the correct tracer/ pathogen combination to be fruitfully used to investigate biological questions, the radiochemistry of the nuclide itself as well as the radiotracer as a whole must be thoroughly understood.

This Page Intentionally Left Blank.